Visualization of Thawing and Desaturation in Frozen Gas Diffusion Layers of Proton Exchange Membrane Fuel Cells via Synchrotron X-ray Computed Tomography

A Thesis Submitted to the College of Graduate and Postdoctoral Studies

in partial fulfillment of the requirements for the degree of

Master of Science

in the Department of Chemical and Biological Engineering

University of Saskatchewan

Saskatoon

By

Yuzhou Zhang

Permission to use

The author has agreed that the Libraries of the University of Saskatchewan may make this thesis freely available for inspection. Moreover, the author has agreed that permission for extensive copying of this thesis for scholarly purposes may be granted by the professor(s) who supervised the thesis work recorded herein or, in their absence, by the Head of the Department of Chemical and Biological Engineering or the Dean of the College of Graduate and Postdoctoral Studies. Copying or publication or any other use of the thesis or parts thereof for financial gain without written approval by the University of Saskatchewan is prohibited. It is also understood that due recognition will be given to the author of this thesis and to the University of Saskatchewan in any use of the material of the thesis.

Requests for permission to copy or to make other use of material in this thesis in whole or in part should be addressed to:

Head of the Department of Chemical and Biological Engineering
University of Saskatchewan
57 Campus Drive
Saskatoon, Saskatchewan
S7N 5A9
Canada

OR

Dean
College of Graduate and Postdoctoral Studies
University of Saskatchewan
116 Thorvaldson Building, 110 Science Place
Saskatoon, Saskatchewan S7N 5C9 Canada

Abstract

Proton exchange membrane fuel cells (PEM fuel cells) are one of the promising clean energy solutions to replace fossil fuel in applications such as automobiles and stationary power systems. Though significant research progress has been made, there are still some key technical challenges to be solved including the water management and cold-start problems, hindering large scale commercialization of this technology. A successful water management requires the amount of water content in a PEM fuel cell system to be kept at an optimal level. A poor water management would lead to membrane dehydration or liquid water flooding, which would cause temporary or permanent losses in performance and durability. The water flooding problem would become more serious in the subzero temperature during the cold-start process, which could lead to irreversible damages on cell components, or even cell failure in some extreme cases. Due to opaque nature of PEM fuel cell components, visualization and understanding of water transport behavior remains a challenge.

Therefore, thawing and desaturation processes of gas diffusion layers (GDLs) under cold-start operating conditions were studied in this research via synchrotron X-ray computed tomography (CT) imaging techniques. The high speed and high resolution CT scan made it possible to capture the dynamic water behavior during the thawing and desaturation process for both qualitative and quantitative analyses. The experiments were performed on a half cell (cathode side) with a 40 mm serpentine channel, where Sigracet® 35AA and 35BA graphite GDLs were selected in different trials, with the superficial gas velocity of the purging air set to 2.88 m/s, 4.26 m/s, 5.98 m/s and 9.02 m/s. A similar desaturation pattern was observed in both global and local GDL regions; however, heterogeneity in water transfer was found over the entire GDL domains, both in-plane and through-plane. It was also found that the air purging rate, purging distance, and flow field geometry would affect the desaturation pattern, while the GDL hydrophobicity would mainly affect the initial saturation level. These data provide valuable information for future experimental and modeling studies that involve the thawing process in the GDL, and could be used to optimize the cell design and develop the cold-start protocols.

Acknowledgements

I would like to thank Dr. Lifeng Zhang as my supervisor from the University of Saskatchewan, and Dr. Ryan Anderson from Montana State University for their continuous support, guidance, and advice during this research.

Next, I would like to thank Dr. Ning Zhu from the Canadian Light Source for his technical support in synchrotron experiments and image processing. I am also grateful to Chen Li, Viral Hirpara, and Virat Patel from my research group for their assistance in synchrotron experiments.

I would also like to thank my committee member Dr. Amira Abdelrasoul for providing valuable suggestions during the research.

Finally, I would like to thank Natural Sciences and Engineering Research Council of Canada (NSERC) and University of Saskatchewan for the financial support on this research.

Table of Contents

List of Figures

List of Tables

Chapter 1. Introduction

Clean energy has received increasing attention nowadays as the key to the sustainable development. Fuel cells are devices to directly convert the chemical potential into electricity, which are considered to be one of the promising clean energy solutions for increased greenhouse gas emissions associated with using fossil fuels. Proton exchange membrane fuel cells (PEM fuel cells) as one type of fuel cells, is of particular interest in the transportation sector because of their high energy efficiency and low operating temperature requirements.

Figure 1.1 shows a schematic model of a single PEM fuel cell. Hydrogen gas and oxygen gas flow into the cell through the bipolar plates separately from the anode side and the cathode side. The gas streams then evenly diffuse to the catalyst layers through gas diffusion layers (GDLs). Two half-electrochemical reactions take place on the two sides, as shown in the equations below.

$$Anode: 2H_2 \rightarrow 4H^+ + 4e^-$$

$$Cathode: O_2 + 4H^+ + 4e^- \rightarrow 2H_2O$$

$$Overall: O_2 + 2H_2 \rightarrow 2H_2O$$

At the anode side, 4 electrons are removed from every 2 hydrogen molecules to form 4 protons. At the cathode side, oxygen gains 4 electrons to form 2 oxygen ions. The protons are transferred through the membrane and react with oxygen to generate water and heat on the cathode side. Electrons are collected through the circuit between the anode side and the cathode side.

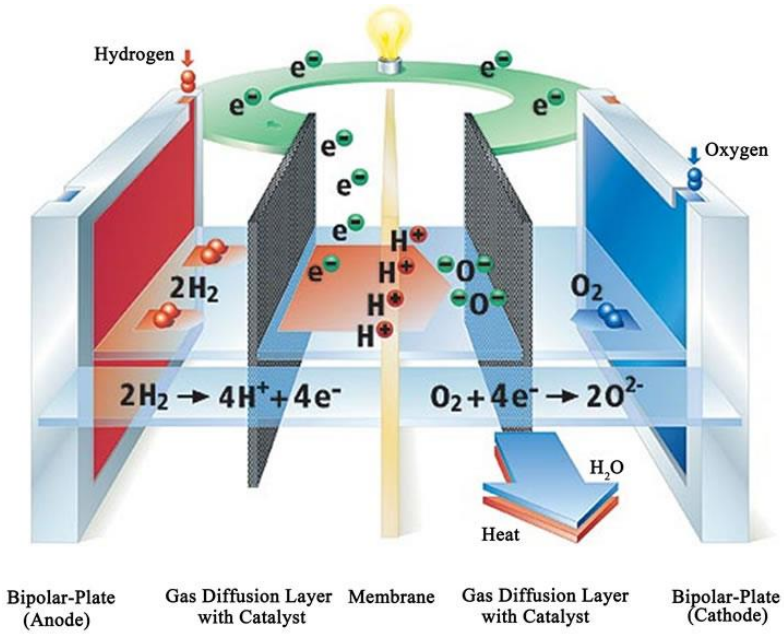

Figure 1.1. A PEM fuel cell single cell [1]

PEM fuel cells are one of the most common type of commercialized fuel cells and receive significant interest due to the following advantages:

1. High energy conversion. Unlike thermodynamic engines limited by the Carnot cycle, PEM fuel cells have 40 % - 60 % energy conversion efficiency from the chemical potential to electricity.
2. Zero emission as water being the only byproduct.
3. Low operating temperatures at 60 °C – 80 °C for normal operation and low noise production compared to other engines.
4. Portability. PEM fuel cells can be scaled up or down by increasing or decreasing the number of cells in a stack. It can be used in small and portable applications such automobiles.

Though great success has been achieved in utilizing PEM fuel cells, there still exist technical challenges hindering massive production and application of this technology. Among them, water management is one of the key challenges in the PEM fuel cell operation and design. An optimal level of water in a PEM fuel cell is vital for its performance and durability, where the cell needs to be humidified to maintain the hydration level, and the excess liquid water needs to be

effectively removed from the cell. A sufficient amount of water is necessary to prevent membrane dehydration, which could lead to performance degradation and permanent material damage [2]. However, accumulation of excess liquid water may cause the mass transfer limitation in GDLs and flow channels, which can lead to performance losses [3]. Specially in the cold-start conditions, when the cell operates in subzero temperatures, the excess liquid water in the catalyst layers, GDLs, and flow channels can freeze rapidly causing mechanical damages such as deformation, delamination, and perforation [4,5]. Also, as the ice completely blocks paths before thawing, the prolonged mass transfer limitation may cause the fuel and oxidant starvation, which could lead to permanent performance and durability loss, or cell failure in extreme cases [6]. Therefore, understanding the water transfer behavior in the PEM fuel cell is critical for better water management and successful cell design.

1.1 Knowledge gap and motivation

For water management in the GDLs, water transfer behaviors are still not fully understood, specially under subzero operating temperatures. From experimental perspectives, in-situ measurements of the effects of the operating parameters for a cold-start PEM fuel cell may provide valuable information to evaluate the overall efficiency of the applied water management protocols, however, it is not enough to characterize the localized water behavior. For modeling and simulation approaches, the complexity in the fuel cell system including microscale and macroscale two/three phase flow, porous media, thermodynamics, phase change, etc. make it difficult to build a working model which represents the actual water transfer in PEM fuel cells at multiple scales.

Visualization techniques such as Synchrotron X-ray could help in studying the water behavior in the localized area. However, most of the existing visualization works about the GDL water management were performed on idle PEM fuel cells, focusing on the GDL structural change or water distribution. The scanning speed could often take several minutes, which is too slow to capture the dynamic water movement. Furthermore, the time sensitivity increases when the cold-start conditions are applied, as the thawing of ice could happen much faster than the scanning speed. Only few experiments which visualized the dynamic water transfer below the melting point only provided low spatial resolution images due to apparatus limitation [7,8].

Base on one previous work performed by Battrell et al. [9] which captured the dynamic water removal process in the initial saturated GDL at room temperature, the cold-start condition was the focus in this project, with improved synchrotron apparatus and experimental setup to increase the quality of images captured. Since Battrell et al. only performed the experiments with one GDL sample and one purging flow rate under the ambient condition, multiple GDL samples and different purging flow rates were examined under the cold-start condition, where the freezing of the residual water and the rapid ice formation during the cold-start were simulated.

1.2 Research objectives

The objective of this research was to provide qualitative and quantitative analysis of the GDL thawing and desaturation process under the cold-start condition via synchrotron X-ray imaging. Several operating parameters including GDL properties, purging flow rates, purging distances and flow field geometries were analyzed at global and local scales in order to understand their effects on the water behavior in the GDL.

1.3 Organization of the thesis

This project produced two published manuscripts. The thesis is written in a manuscript-based style with five chapters. Chapter 1 includes the introduction, along with knowledge gap, motivation, research objectives, and thesis organization. Literature review on PEM fuel cell water management, gas diffusion layer, cold-start, and visualization techniques are presented in Chapter 2. Chapter 3 contains the first published manuscript which analyzed the thawing and desaturation process of the cold-start GDLs, focused on the global scale. Based on the results and problems discovered in Chapter 3, Chapter 4 contains the second published manuscript which further analyzed the GDL cold-start at the local scale. Chapter 5 discusses the main conclusions drawn from this project and recommendations provided for future research. The references are provided at the end of each associated chapter.

1.4 References

[1] Garraín, Daniel, Yolanda Lechón, and Cristina de Rúa. “Polymer Electrolyte Membrane Fuel Cells (PEMFC) in Automotive Applications: Environmental Relevance of the

Manufacturing Stage." *Smart Grid and Renewable Energy* 02, no. 02 (2011): 68–74. https://doi.org/10.4236/sgre.2011.22009.

[2] Wu, Jinfeng, Xiao Zi Yuan, Jonathan J. Martin, Haijiang Wang, Jiujun Zhang, Jun Shen, Shaohong Wu, and Walter Merida. "A Review of Pem Fuel Cell Durability: Degradation Mechanisms and Mitigation Strategies." *Journal of Power Sources* 184, no. 1 (2008): 104–19. https://doi.org/10.1016/j.jpowsour.2008.06.006.

[3] Mench, Matthew M. *Fuel Cell Engines*. Hoboken, NJ: Wiley, 2008.

[4] Kim, S., and M.M. Mench. "Physical Degradation of Membrane Electrode Assemblies Undergoing Freeze/Thaw Cycling: Micro-Structure Effects." *Journal of Power Sources* 174, no. 1 (2007): 206–20. https://doi.org/10.1016/j.jpowsour.2007.08.111.

[5] Lee, Sang-Yeop, Hyoung-Juhn Kim, EunAe Cho, Kug-Seung Lee, Tae-Hoon Lim, In Chul Hwang, and Jong Hyun Jang. "Performance Degradation and Microstructure Changes in Freeze–Thaw Cycling for PEMFC MEAs with Various Initial Microstructures." *International Journal of Hydrogen Energy* 35, no. 23 (2010): 12888–96. https://doi.org/10.1016/j.ijhydene.2010.08.070.

[6] Kim, Soowhan, Byung Ki Ahn, and M.M. Mench. "Physical Degradation of Membrane Electrode Assemblies Undergoing Freeze/Thaw Cycling: Diffusion Media Effects." *Journal of Power Sources* 179, no. 1 (2008): 140–46. https://doi.org/10.1016/j.jpowsour.2007.12.114.

[7] Siegwart, M., F. Huang, M. Cochet, T. J. Schmidt, J. Zhang, and P. Boillat. "Spatially Resolved Analysis of Freezing during Isothermal PEFC Cold Starts with Time-of-Flight Neutron Imaging." *Journal of The Electrochemical Society* 167, no. 6 (2020): 064510. https://doi.org/10.1149/1945-7111/ab7d91.

[8] Oberholzer, P., P. Boillat, R. Siegrist, R. Perego, A. Kästner, E. Lehmann, G. G. Scherer, and A. Wokaun. "Cold-Start of a PEFC Visualized with High Resolution Dynamic In-

Plane Neutron Imaging." *Journal of The Electrochemical Society* 159, no. 2 (2011). https://doi.org/10.1149/2.085202jes.

[9] Battrell, Logan, Virat Patel, Ning Zhu, Lifeng Zhang, and Ryan Anderson. "Imaging of the Desaturation of Gas Diffusion Layers by Synchrotron Computed Tomography." *Journal of Power Sources* 416 (2019): 155–62. https://doi.org/10.1016/j.jpowsour.2019.01.089.

Chapter 2. Literature Review

2.1 PEM fuel cell water management

For better fuel cell performance and steady fuel cell operation, the water content within the fuel cell system needs to be maintained in an optimal range. In general, the influences of water content on the PEM fuel cell can be summarized as follows [1]:

1. Membrane electrode assembly (MEA) must be maintained in hydration state during the operation since the water content is proportional to the conductivity of the electrolyte. Insufficient water content would increase the ohmic resistance which would lead to cell performance loss.
2. Extra liquid water may flood the catalyst layer and block the mass transfer to the active sites. However, insufficient water would decrease the catalyst activity.
3. Liquid water may flood the GDL and block the pores which connect the gas channels and the catalyst layers. It will induce the mass transfer limitation to the active sites which leads to performance loss.
4. Excess liquid water may block the gas channels. It may cause the fuel or oxidant starvation, which may lead to performance loss, cell voltage reversal, and unwanted side reactions.
5. The reaction rate may be reduced as the reactants stream been diluted when there is too much water vapor in the system.

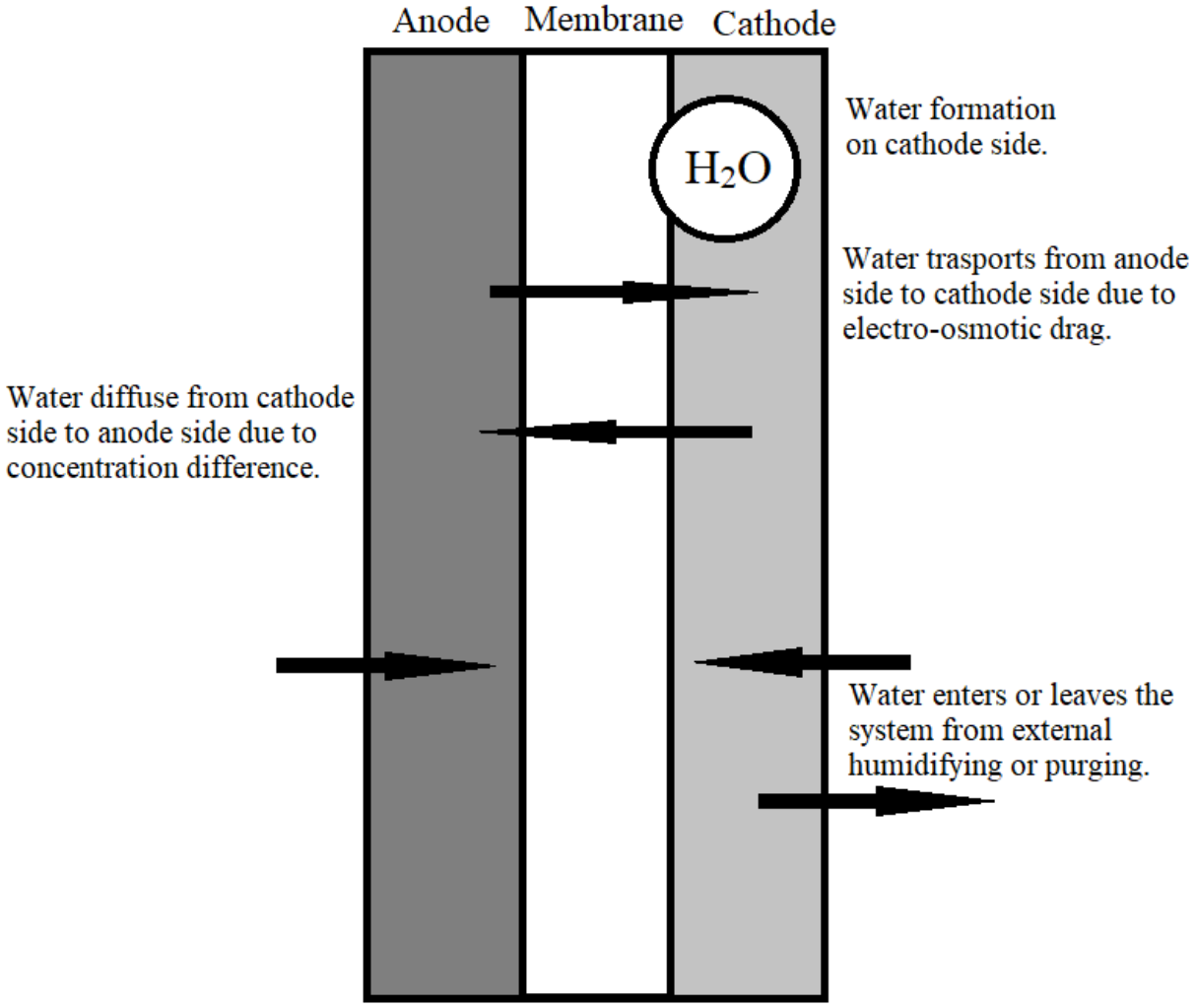

Figure 2.1. PEMFC different water movements through the electrolyte

As shown in Figure 2.1, water content could be transferred in the PEM fuel cell system in the following ways [2]:

1. Water formation on the cathode side as the product during the electrochemical reaction.
2. Due to electro-osmotic drag, water on the anode side will continuously transport into the cathode side during operation. For every 1 hydrogen ion, about 1 ~ 5 water molecules will be carried to the cathode side through the membrane.
3. Water may diffuse from the cathode side to the anode side due to the concentration difference.

4. Water content would be introduced from and purged to the external system. Fuel and oxidant streams are usually humidified at the inlet to prevent fuel cell dehydration. Also, excess liquid water has to be removed from the fuel cell system to prevent liquid water buildup.

In the normal operating temperature (higher than 60°C), only considering the internal water transfer, the drying effect from the gas streams would usually be higher than the water production rate from the electrochemical reaction, where the PEM fuel cell would naturally be dehydrated during the operation. It can often be overcome with the pre-humidifying protocol to increase the humidity of the gas streams up to 100 %. Methods such as direct water injection, water bubbler humidifier, and water recycle system can be applied to either oxygen or hydrogen stream, or sometime both streams, depending on the operating conditions.

On the other hand, in the low operating temperature, the water production would often be higher than the water removal rate, especially at high current density. Also, due to water transfer through the membrane, water content may build up in the cathode side when the anode side remains in the optimum hydration range. Water flooding would occur in various components of PEM fuel cells and reduce the mass transfer rate of the reactant gas. Therefore, additional purging with high velocity dry gas may be applied to remove the excess water from the system.

To achieve high performance, the water content in the PEM fuel cell system needs to be balanced for sufficient membrane hydration and low water flooding. The complexity of the microscale transfer phenomena and the liquid/gas two-phase flow in the fuel cell system poses challenges on fully understanding the water behaviors through the modeling and experiments. Therefore, water management is still one of the key challenges for PEM fuel cell commercialization.

2.2 Gas diffusion layers

Gas diffusion layers (GDLs) are one of the key components in PEM fuel cell stacks. As a thin conductive porous media layer placed between the bipolar plate and the catalyst layer/membrane, the GDL has multiple functions: bridge of mass transfer between the channel and catalyst layer which ensures even gas distribution and fast water removal, heat transfer media during the cell operation; electrodes which transfer electrons between the catalyst layer and the

bipolar plate; and structure support for the catalyst and membrane. Playing a critical role in water management, GDLs help the excess water content being removed from the reaction sites through its porous channels. Poor water management could sometime lead to water flooding in the GDL and block the gas diffusion to the catalyst layer, which then limits the cell performance.

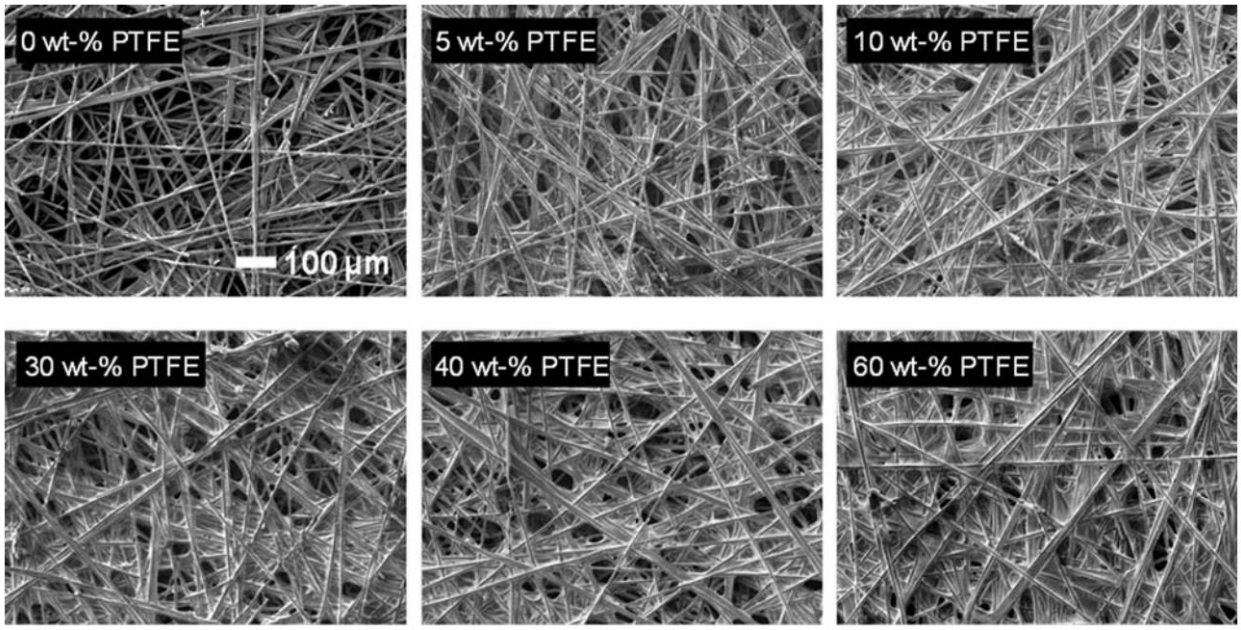

Figure 2.2. Scanning-electron microscope (SEM) images of TGP-120 GDL with various PTFE loadings [3] (With permission from IOP Publishing, Ltd.)

In the current design, GDLs used in PEM fuel cells are commonly made of carbon fibers as shown in Figure 2.2, owning to its high porosity (75 % - 90 %), excellent electrical and heat conductivity. In production, GDLs are often integrated with the catalyst layers and membrane into the membrane electrode assembly (MEA). Polytetrafluoroethylene (PTFE) treatment could be applied on carbon fibers to increase the GDL hydrophobicity. Also, the microporous layer (MPL) could be coated on the surface of GDLs to decrease the water droplet size closed to the catalyst layer and reduce the GDL saturation. Combining these two treatments, liquid water could be quickly removed to prevent the water buildup during the high current operation.

2.3 Operation under subzero temperature and cold-start

Automobile is one of the most interested applications for commercialized PEM fuel cells. To replace with the fossil fuel engines, PEM fuel cells are required to normally operate in different

conditions including the subzero temperature range. In the normal operation phase, heat generates during the electrochemical reaction would overcome the cold surrounding temperature to remain a high temperature in fuel cells. However, in the start-up phase under cold weather, the fuel cell would operate below 0°C. The residual water from the shut-down phase and the generated water during the start-up phase would freeze in the channels, GDLs, catalyst layers and will not be quickly removed until the cell reaches above 0°C. The following problems may occur due to the ice formation:

1. The volume expansion due to freezing may cause the mechanical damage on the PEM fuel cell, such as cracking and piercing on the bipolar plates and MEAs. These mechanical damages may cause the temporary or permanent performance degradation, or in more serious cases, cause leakage and lead to failure on the entire fuel cell [4].

2. Similar to the water flooding, the solid ice in the PEM fuel cell could limit the mass transfer and then decrease the cell performance. However, the ice blockage may last for serval minutes during the cold-start. A massive ice formation may cause the fuel or air starvation as reactants being used up due to the blockage, and in consequence, cause cell reversal. It is a phenomenon that the electric potential of the fuel cell decreases or even becomes negative. Instead of generating power, the fuel cell would consume electricity from the battery. Side reactions such as the carbon corrosion would dominate the reactions. It may lead to irreversible cell damage on the catalyst, membrane, GDL or even the bipolar plate [5]. The cell reversal may happen in normal operating conditions due to uneven gas distribution or flooding. It would become a more serious problem in cold start due to the long-lasting ice blockage.

For the ice formation related to the residual water, gas purging is considered to be the most effective solution. High velocity, high pressure dry gas stream (reactants stream or nitrogen) would flow through the cells during the shut-down phase to remove the majority of the liquid water from the channels and the MEAs. For the generated water during the cold-start, heating is usually applied to the fuel cell stack to reduce the operating time below the freezing point. Methods including the external heating (using the external heating sources such as hot coolant or heating coils) and the internal heating (using the heat generated within the stack) could be applied to quickly increase the stack temperature [6].

2.4 Visualization techniques on PEM fuel cell

To qualitatively or quantitatively study the PEM fuel cell water management from experiments, two approaches are commonly used. One approach focuses on the in-situ measurement of PEM fuel cell parameters including voltage, current, flow rate, pressure, humidity, heat generation and then evaluate the overall water management base on the cell performance. The other approach is in-situ visualization, by which the water transfer is directly observed in areas of interest. The overall water management of the PEM fuel cell may not be captured through visualization due to the limited field of view, however the water behavior can be observed inside of the cell components within a localized area. Liquid water in PEM fuel cells can be observed using the visualization techniques including optical photography, nuclear magnetic resonance, neutron imaging, and X-ray imaging [7].

2.4.1 Optical photography

Optical photography can be applied by directly viewing PEM fuel cells through the microscope or cameras. It can provide the real time information about the dynamic change of liquid water in the flow field and the surface of GDL, when varying the operating parameters. The cell components (i.e.: bipolar plates) need to be replaced by the transparent material in order to observe the water behavior in-situ. The spatial and temporal resolution are only limited by the microscope magnification and the camera capture speed. The resolutions of the optical approaches are usually lower than the other visualization methods.

2.4.2 Nuclear magnetic resonance (NMR)

In nuclear magnetic resonance (NMR), the emitted radio-frequency signal from the special atomic nuclei is collected to provide the image contrast. The specific atomic nuclei with non-zero spin moments such as 1H would be excited by a strong static magnetic field and absorb a radio-frequency signal. The excited nuclei would then resonate at a detectable frequency which is proportional to the applied magnetic field [8]. In study the water distribution in the PEM fuel cell, the presence of water molecules can be detected by measuring the resonated radio-frequency signal from the exited 1H, where an example is shown in Figure 2.3. The in-plane spatial resolution of the NMR is limited to 400 x 25 μm, and the temporal resolution is limited to 50 s [9]. NMR can provide useful data in imaging the water content in the gas channels and membrane; however, it is limited by the low resolution, and it is incompatible with the carbon materials such as GDLs [10].

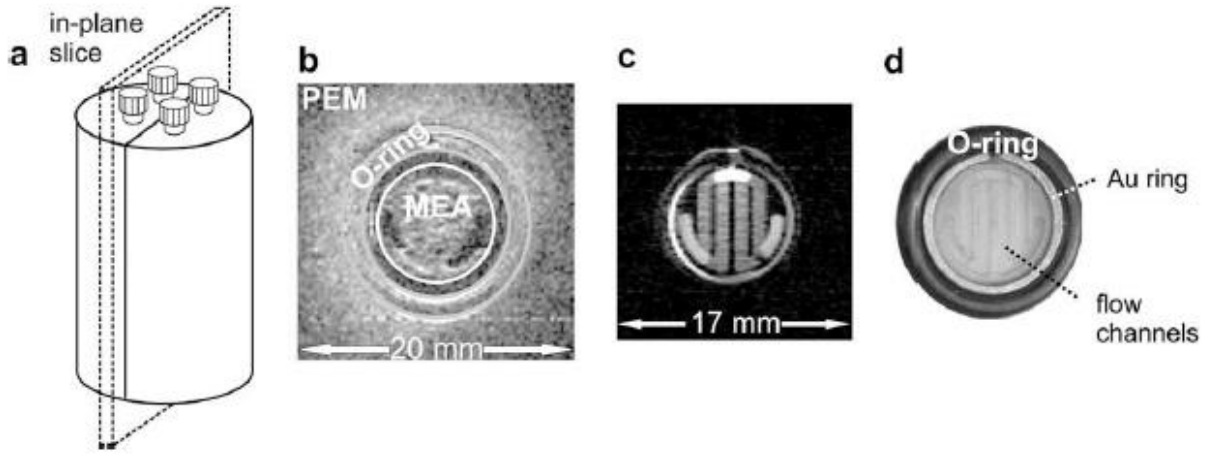

Figure 2.3. ^{1}H NMR microscopy apparatus for PEM fuel cell investigation and sample images reported by Feindel et al. [10]: (a) PEM fuel cell schematic, (b) 500 mm slice image containing the MEA, (c) 750 mm slice image containing a water filled flow field, and (d) photograph of the fuel cell cross-section. (With permission from Royal Society of Chemistry)

2.4.3 Neutron imaging

Neutron imaging measures the attenuation of the neutron beam after it passes the scanned object and the attenuations for different materials are based on their neutron attenuating properties. The attenuation of the signal is proportional to the material composition. As the example shown in Figure 2.4, the neutron imaging technique is suitable for visualizing the water content in the PEM fuel cell and GDL due to the neutron's sensitivity of hydrogen containing compound such as water, and is insensitive to the cell materials such as graphite [11]. The neutron imaging can provide a spatial resolution of 100 x 100 μm, and the temporal resolution is limited to 5.4 s [12,13]. These resolutions are insufficient to study the through-plane water transfer and the water droplet movement. For in-plane visualization, it is difficult to distinguish the presence of water in the GDL from the water in the flow channels [14]. Neutron imaging is also limited by its availability and cost, since it requires a nuclear reactor as the neutron source.

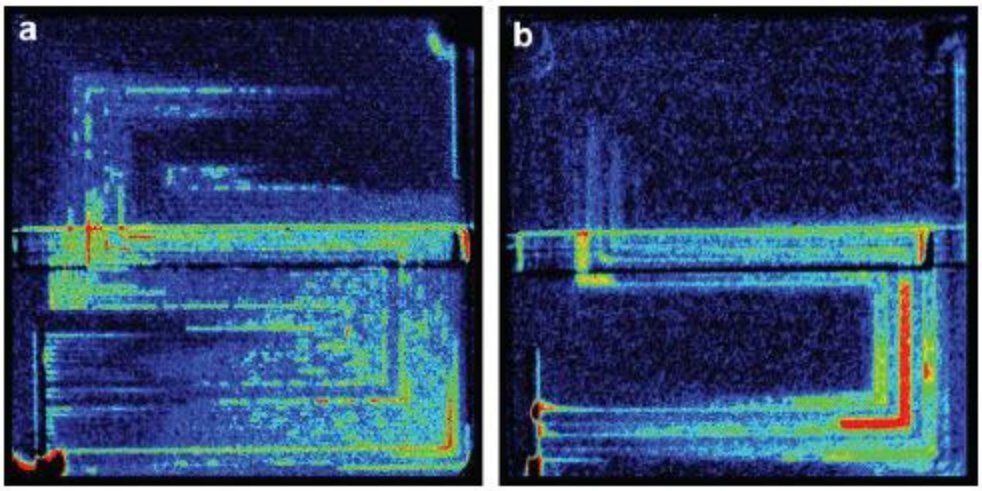

Figure 2.4. Neutron images for a PEM fuel cell reported by Turhan et al. [15] with (a) 48 channel-GDL interfaces and (b) 12 channel-GDL interfaces at a current density of 0.2 A/cm^2 showing the increase in liquid water accumulation associated with a higher number of channel-GDL interfaces. (With permission from Elsevier)

2.4.4 X-ray imaging

Similar to neutron imaging, X-ray imaging measures the attenuated X-ray beam after it travels through the scanned object and is partially absorbed by the materials, where the attenuations are based on the density of the materials. By measuring the transmitted signal, X-ray imaging can provide a three-dimensional map of adsorption within the sample. This technique has been used in studying the water distribution in the PEM fuel cell and the GDL structure, due to that the contrast could be provided through a density difference between liquid water/cell materials and vacant volume (gas). By employing synchrotron as the X-ray source for visualization, the scanning speed can be greatly increased due to its the high photon flux. The spatial resolution of the synchrotron X-ray imaging is reported as 3-7 μm, and the temporal resolution is 4.8 s, according to the literature [16].

In PEM fuel cell visualization studies, computed tomography (CT) is commonly applied along with X-ray imaging. By taking multiple scans in different angles of a sample, the 2D projections can be reconstructed into 3D tomographic images. As shown in Figure 2.5, the more projections taken in each CT would increase the quality and accuracy of the 3D images. In visualizing the water management, applying CT scan makes it possible to observe the inside of the cell without physically cutting it. Combined with the contrast difference, the 3D tomographic

images can be segmented into different sections such as liquid water, GDL fiber, MPL to obtain the 3D geometry model, as shown in Figure 2.6.

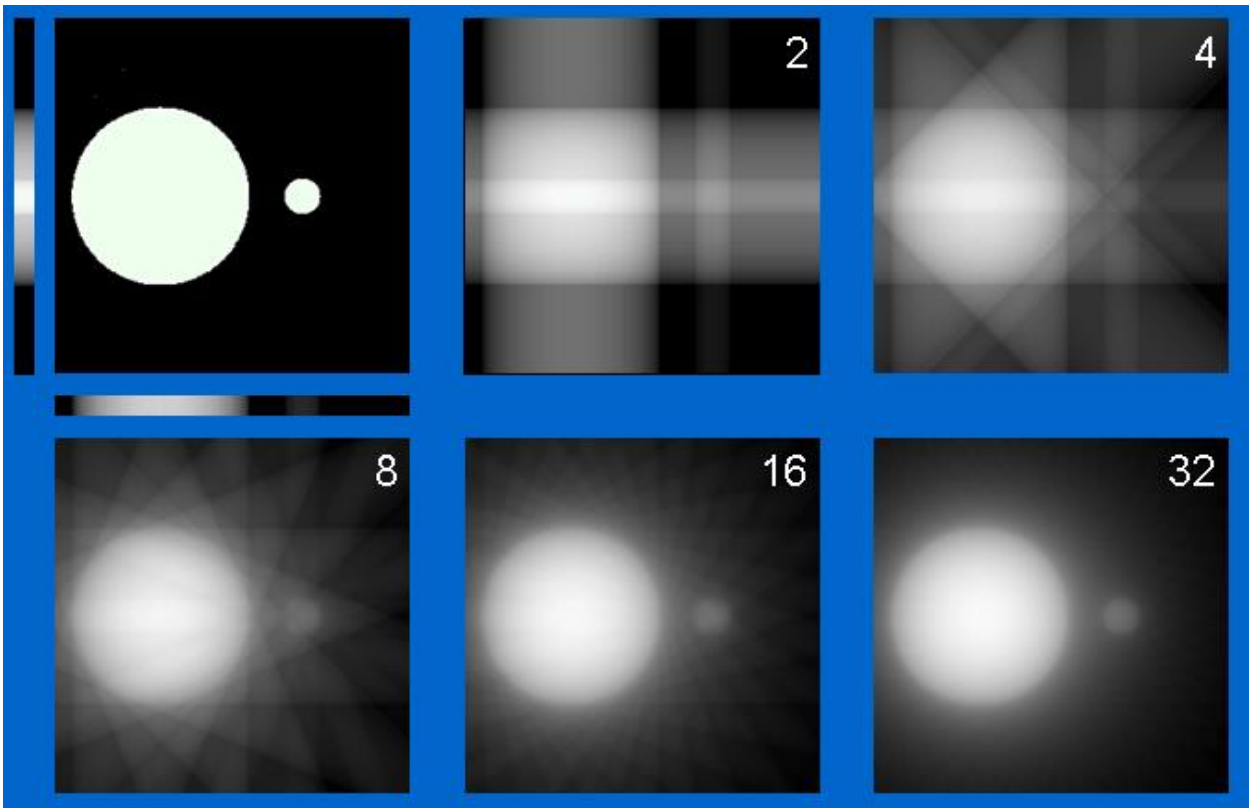

Figure 2.5. Demonstration of the increased image quality for the reconstructed CT as the number of projections increases from 2 to 32 [17].

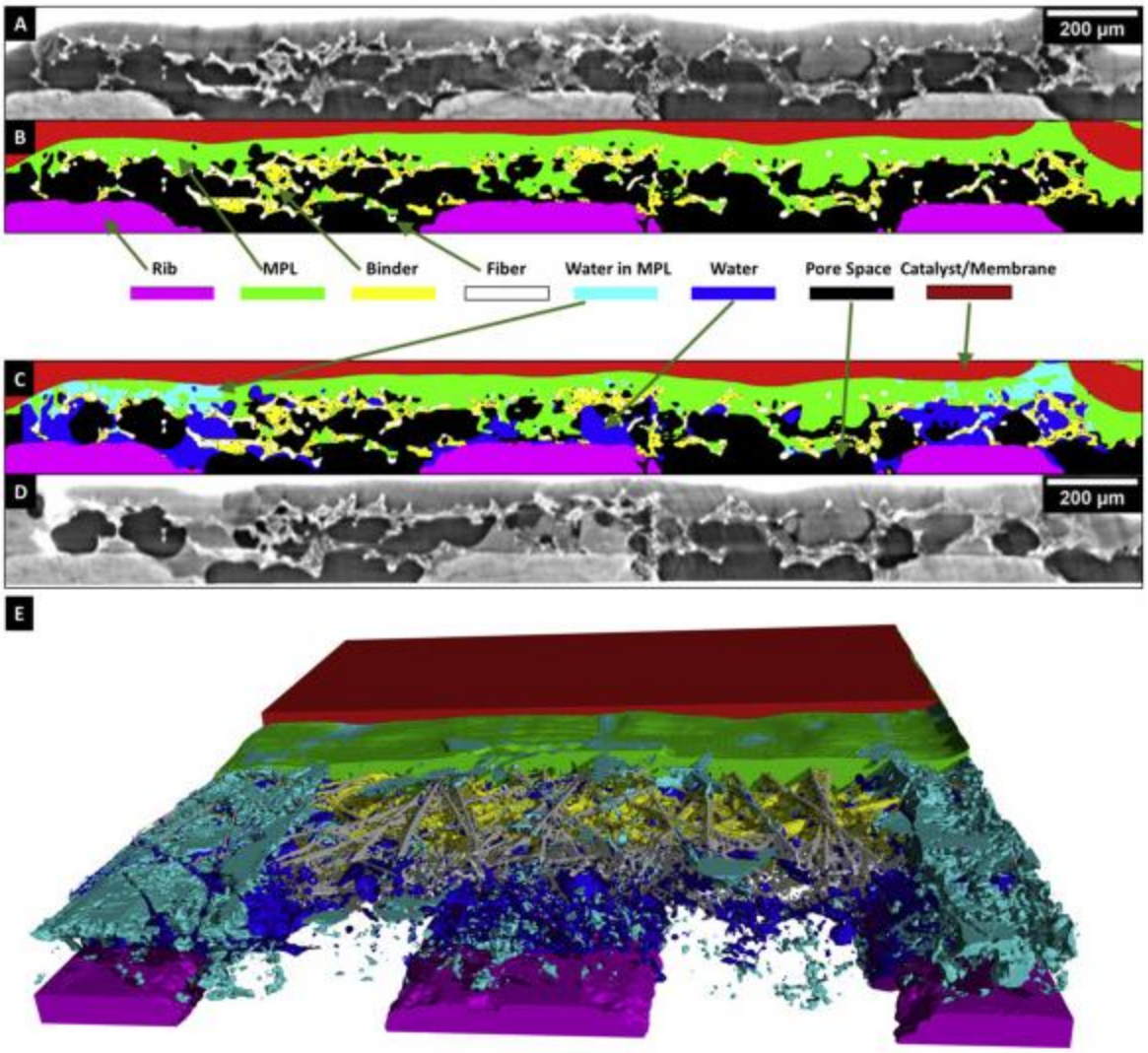

Figure 2.6. Classification result for the dry and operated cell states. A: dry state input, B: classified dry state, C: classified operated state, D: operated input, E: All classified fuel cell materials in 3D-view [18]. (With permission from Elsevier)

Several existing studies via synchrotron X-ray imaging have proved that this visualization technique is capable of studying the GDL water management and PEM fuel cell cold-start. Zenyuk et al. [19] measured the water evaporation rates for several GDLs with the conditions of 200 and 600 ml/min gas flow rate at 30 °C, using the 3D water mesh segmented from X-ray CT images. Battrell et al. [20,21] visualized the desaturation process of the saturated GDLs both in global and localized areas, assessing convection and evaporation with 50 ml/min gas flow rate. Otsuki et al. [22] measured the solidification heat from supercooled water using thin-film thermocouples and

visualized the ice distribution via X-ray CT after several cold-start operations. By in-situ visualization of water production and water transfer via synchrotron X-ray CT, Mayrhuber et al. [23] investigated the mechanism of the performance drop during the cold-start operation of PEM fuel cells.

2.5 References

[1] Ji, Mengbo, and Zidong Wei. "A Review of Water Management in Polymer Electrolyte Membrane Fuel Cells." *Energies* 2, no. 4 (2009): 1057–1106. https://doi.org/10.3390/en20401057.

[2] Larminie, James, and Andrew L. Dicks. *Fuel Cell Systems Explained*. Chichester: Wiley, 2003.

[3] Santamaria, Anthony D., Prodip K. Das, James C. MacDonald, and Adam Z. Weber. "Liquid-Water Interactions with Gas-Diffusion-Layer Surfaces." *Journal of The Electrochemical Society* 161, no. 12 (2014). https://doi.org/10.1149/2.0321412jes.

[4] Oh, Yumi, Sang-Kyung Kim, Seongyop Lim, Doo-Hwan Jung, Dong-Hyun Peck, and Yonggun Shul. "The Effects of Freeze-Thaw Cycling and Gas Purging on Performance Degradation in Direct Methanol Fuel Cells." *International Journal of Hydrogen Energy* 37, no. 22 (2012): 17268–74. https://doi.org/10.1016/j.ijhydene.2012.08.081.

[5] Qin, Congwei, Jue Wang, Daijun Yang, Bing Li, and Cunman Zhang. "Proton Exchange Membrane Fuel Cell Reversal: A Review." *Catalysts* 6, no. 12 (2016): 197. https://doi.org/10.3390/catal6120197.

[6] Amamou, Ali Akrem, Sousso Kelouwani, Loic Boulon, and Kodjo Agbossou. "A Comprehensive Review of Solutions and Strategies for Cold Start of Automotive Proton Exchange Membrane Fuel Cells." *IEEE Access* 4 (2016): 4989–5002. https://doi.org/10.1109/access.2016.2597058.

[7] Bazylak, A. “Liquid Water Visualization in PEM Fuel Cells: A Review.” *International Journal of Hydrogen Energy* 34, no. 9 (2009): 3845–57. https://doi.org/10.1016/j.ijhydene.2009.02.084.

[8] St-Pierre, Jean. “PEMFC In Situ Liquid-Water-Content Monitoring Status.” *Journal of The Electrochemical Society* 154, no. 7 (2007). https://doi.org/10.1149/1.2737542.

[9] Tsushima, Shohji, Kazuhiro Teranishi, and Shuichiro Hirai. “Magnetic Resonance Imaging of the Water Distribution within a Polymer Electrolyte Membrane in Fuel Cells.” *Electrochemical and Solid-State Letters* 7, no. 9 (2004). https://doi.org/10.1149/1.1774971.

[10] Feindel, Kirk W., Steven H. Bergens, and Roderick E. Wasylishen. “The Influence of Membrane Electrode Assembly Water Content on the Performance of a Polymer Electrolyte Membrane Fuel Cell as Investigated by 1H NMR Microscopy.” *Physical Chemistry Chemical Physics* 9, no. 15 (2007): 1850. https://doi.org/10.1039/b617551a.

[11] Satija, R., D.L. Jacobson, M. Arif, and S.A. Werner. “In Situ Neutron Imaging Technique for Evaluation of Water Management Systems in Operating PEM Fuel Cells.” *Journal of Power Sources* 129, no. 2 (2004): 238–45. https://doi.org/10.1016/j.jpowsour.2003.11.068.

[12] Kim, Soowhan, and M. M. Mench. “Investigation of Temperature-Driven Water Transport in Polymer Electrolyte Fuel Cell: Phase-Change-Induced Flow.” *Journal of The Electrochemical Society* 156, no. 3 (2009). https://doi.org/10.1149/1.3046136.

[13] Owejan, J.P., T.A. Trabold, J.J. Gagliardo, D.L. Jacobson, R.N. Carter, D.S. Hussey, and M. Arif. “Voltage Instability in a Simulated Fuel Cell Stack Correlated to Cathode Water Accumulation.” *Journal of Power Sources* 171, no. 2 (2007): 626–33. https://doi.org/10.1016/j.jpowsour.2007.06.174.

[14] Kowal, J. J., A. Turhan, K. Heller, J. Brenizer, and M. M. Mench. “Liquid Water Storage, Distribution, and Removal from Diffusion Media in PEFCS.” *Journal of The Electrochemical Society* 153, no. 10 (2006). https://doi.org/10.1149/1.2258049.

[15] Turhan, A., K. Heller, J.S. Brenizer, and M.M. Mench. “Passive Control of Liquid Water Storage and Distribution in a PEFC through Flow-Field Design.” *Journal of Power Sources* 180, no. 2 (2008): 773–83. https://doi.org/10.1016/j.jpowsour.2008.02.028.

[16] Manke, I., Ch. Hartnig, M. Grünerbel, W. Lehnert, N. Kardjilov, A. Haibel, A. Hilger, J. Banhart, and H. Riesemeier. “Investigation of Water Evolution and Transport in Fuel Cells with High Resolution Synchrotron x-Ray Radiography.” *Applied Physics Letters* 90, no. 17 (2007): 174105. https://doi.org/10.1063/1.2731440.

[17] Platten, David. “Basic Principles of CT Scanning.” ImPACT. http://www.impactscan.org/slides/impactcourse/basic_principles_of_ct/index.html.

[18] Ince, Utku U., Henning Markötter, Nan Ge, Merle Klages, Jan Haußmann, Martin Göbel, Joachim Scholta, Aimy Bazylak, and Ingo Manke. “3D Classification of Polymer Electrolyte Membrane Fuel Cell Materials from in-Situ X-Ray Tomographic Datasets.” *International Journal of Hydrogen Energy* 45, no. 21 (2020): 12161–69. https://doi.org/10.1016/j.ijhydene.2020.02.136.

[19] Zenyuk, Iryna V., Adrien Lamibrac, Jens Eller, Dilworth Y. Parkinson, Federica Marone, Felix N. Büchi, and Adam Z. Weber. “Investigating Evaporation in Gas Diffusion Layers for Fuel Cells with X-Ray Computed Tomography.” *The Journal of Physical Chemistry C* 120, no. 50 (2016): 28701–11. https://doi.org/10.1021/acs.jpcc.6b10658.

[20] Battrell, Logan, Ning Zhu, Lifeng Zhang, and Ryan Anderson. “Transient, Spatially Resolved Desaturation of Gas Diffusion Layers Measured via Synchrotron Visualization.” *International Journal of Hydrogen Energy* 43, no. 24 (2018): 11234–43. https://doi.org/10.1016/j.ijhydene.2018.05.017.

[21] Battrell, Logan, Virat Patel, Ning Zhu, Lifeng Zhang, and Ryan Anderson. “Imaging of the Desaturation of Gas Diffusion Layers by Synchrotron Computed Tomography.” *Journal of Power Sources* 416 (2019): 155–62. https://doi.org/10.1016/j.jpowsour.2019.01.089.

[22] Otsuki, Yota, Yusuke Tamada, Shoki Inoue, Kaito Shigemasa, and Takuto Araki. "Measurement of Solidification Heat from Supercooled Water Freezing during PEFC Cold Start and Visualization of Ice Distribution." *International Journal of Hydrogen Energy* 45, no. 31 (2020): 15600–15610. https://doi.org/10.1016/j.ijhydene.2020.04.004.

[23] Mayrhuber, Immanuel, Federica Marone, Marco Stampanoni, Thomas J. Schmidt, and Felix N. Büchi. "Fast X-Ray Tomographic Microscopy: Investigating Mechanisms of Performance Drop during Freeze Starts of Polymer Electrolyte Fuel Cells." *ChemElectroChem* 2, no. 10 (2015): 1551–59. https://doi.org/10.1002/celc.201500132.

Chapter 3. Imaging of Desaturation of the Frozen Gas Diffusion Layers by Synchrotron X-ray Radiography

The contents of this chapter have been published at *International Journal of Hydrogen Energy*.

Citation information:

Zhang, Yuzhou, Viral Hirpara, Virat Patel, Chen Li, Ryan Anderson, Ning Zhu, and Lifeng Zhang. "Imaging of Desaturation of the Frozen Gas Diffusion Layers by Synchrotron X-Ray Radiography." *International Journal of Hydrogen Energy*, 2021. https://doi.org/10.1016/j.ijhydene.2021.02.197.

Contribution of the MSc student

The experiments, data analysis, and manuscript preparation were performed by Yuzhou Zhang. Viral Hirpara, Virat Patel, and Chen Li provided assistance in synchrotron experiments. Ning Zhu provided technical support in synchrotron related problems. Lifeng Zhang and Ryan Anderson provided technical and editorial guidance through the research and manuscript preparation. Lifeng Zhang also provided supervision through the research.

Contribution of this chapter to the overall study

In this chapter, the water removal in a cold-start GDL was visualized via synchrotron X-ray imaging. Both qualitative and quantitative analysis were performed on the thawing and desaturation process, with multiple air purging rates and GDL hydrophobicity employed as controlled parameters. Dynamic colormaps and 3D geometry models were constructed to study the heterogeneity of GDL water transfer during the thawing and desaturation process.

3.1 Abstract

The visualization of the thawing and desaturation process on an initially saturated, frozen gas diffusion layer (GDL) with a serpentine gas flow channel was performed based on synchrotron X-ray computed tomography images. High speed CT scanning during the experiments allowed the dynamic desaturation process to be quantified under the cold-start with air purging condition. The saturation profiles and the desaturation rates were studied over the entire GDL domain, through-plane, and in selected regions of interest for localized behavior. Sigracet® 35AA and 35BA GDLs were selected for the experiments to study the effects of GDL

hydrophobicity. Along with the real-time saturation profiles, the average desaturation rates for the entire GDL domain over the whole purging process were 0.000186 μL cm^{-2} s^{-1}, 0.000470 μL cm^{-2} s^{-1}, 0.000516 μL cm^{-2} s^{-1} and 0.000901 μL cm^{-2} s^{-1} with the superficial gas velocity of the purging air at 2.88 m/s, 4.26 m/s, 5.98 m/s and 9.02 m/s, respectively. In addition, the dynamic saturation contours and 3-D GDL geometry models were constructed to show the liquid water movement through a GDL. Although the GDL desaturation curves for each experiment share similar trends, the results show that different conditions including air flow rate, GDL geometric location, initial water saturation, and GDL boundary condition could cause heterogeneous desaturation behavior on both overall and localized GDL regions. These data provide valuable information for future modeling studies that involve the thawing process in the GDL, and could be used to optimize the cell design and develop cold-start protocols.

Keywords: PEM fuel cell, gas diffusion layer, X-ray radiography, cold-start, desaturation, heterogeneity

3.2 Introduction

Proton-exchange membrane fuel cells (PEMFCs) are considered as a promising solution to replace fossil fuel engines in applications such as automobiles and backup power, owing to their high energy efficiency, zero local emissions, and low operating temperature (50 - 100 °C) [1-6]. The key components of a single PEM fuel cell included the ionic membrane, an anode and cathode catalyst layer, gas diffusion layer (GDL), and gas channels. Hydrogen and oxygen gas are introduced to the anode side and cathode side gas channels separately, then diffuse through the GDLs to the catalyst layers. The reaction is an exothermic electrochemical reaction with production of water on the cathode side. Water management is essential in fuel cell operation and remains one of the major challenges for a successful PEM fuel cell design. Sufficient water is favorable in the PEM fuel cell to prevent performance loss and cell degradation from membrane dehydration, but excess water must be removed from the PEM fuel cell to prevent water blockage [7,8].

In applications such as automobiles, the fuel cell is required to start up and operate in various environments such as subzero temperature. For instance, the Department of Energy in the United States set the target of achieving successful unassisted cold-start from – 30 °C, and General Motors Corporation aimed for unassisted cold-start from – 40 °C [5-9]. Under the

subzero temperature, the residual water in the fuel cell system can freeze with volume expansion, which can lead to irreversible cell performance loss due to physical damage of the cell components [10-13]. In low temperature operation, ice in the channels and the membrane electrode assembly (MEA) could limit or even completely block the reactant gas from reaching the catalysts. It could lead to the gas starvation, where the reactant gas supplies fail to meet the stoichiometric requirements of the fuel cell. Consequences such as carbon corrosion, catalyst degradation, and cell reversal could occur due to gas starvation, and in the long term this reduces the lifetime of the fuel cell or causes cell failure [14-19]. Purging on the anode and/or cathode side is a common solution for the cold-start problem, where the residual water is removed with the pressurized dry gas streams such as air or N_2 [20-22]. As the bridge of water and gas transfer between the channels and the catalyst layers, water management in GDLs had received increasing attention in research, both in experimental and numerical methods. However, the water transfer phenomena in this porous media is still not well understood.

In experimental studies, water management in GDLs generally has two approaches. One of them focuses on measuring parameters such as current density, voltage, pressure, humidity, and heat transfer on the operating PEM fuel cell or stack to evaluate the efficiency of the water management [23-26]. The other method focuses on the localized water transfer phenomenon and its effects insides the pores of the GDLs. Visualization techniques such as X-ray microtomography, which measures the absorbed photon signals as it travels through the samples based on the mass attenuation coefficient of the materials, supports quantitative and qualitative measurements of the distribution and dynamic movement of water inside the GDLs [27-32,35-37]. The high photon flux synchrotron X-ray and the computed tomography (CT) technique makes it possible to capture high spatial and temporal resolution three-dimensional images for the dynamic water transfer process [32]. Compared with the conventional X-ray CT, the high speed synchrotron based CT scan significantly increases the accuracy in capturing the water distribution by reducing the scanning time required for each CT as the motion artifacts from the liquid water movement within a single CT scan can be minimized.

Using synchrotron X-ray CT, numerous studies have visualized water in the GDL, though most of these studies have focused on above freezing temperature conditions. Lamibrac et al. [27] characterized the liquid water saturation as a function of the capillary pressure from X-ray

CT data for the microporous layer (MPL) coated GDLs. The effects of GDL compression on the water distribution was studied by Ince et al. [35], which showed that the in-plane water distribution increased in both MPL and GDL porous structure as the compression level increased. Research by Markötter et al. [36] visualized the increased hydrophilicity in water distribution around the holes of perforated GDLs. Zenyuk et al. [29] measured the water evaporation rates for several GDLs with the conditions of 200 and 600 ml/min gas flow rate at 30 °C, using the 3D water mesh segmented from the X-ray CT images. Battrell et al. [30,37] visualized the desaturation process of the saturated GDLs both in global and localized areas, assessing convection and evaporation with 50 ml/min gas flow rate.

Several visualization studies have also focused on the subzero temperature conditions, or on the freezing/thawing process in GDLs. Siegwart et al. [7] demonstrated the methods for visualizing the dynamic phase change of water in 2D during the isothermal PEM fuel cell cold-start using neutron imaging, where ice was successfully distinguished from liquid water via contrast difference. Oberholzer et al. [38] visualized water accumulation during the isothermal cold-start with in-plane neutron imaging. Otsuki et al. [39] conducted in-situ measurements of the solidification heat from supercooled water using the thin-film thermocouples and visualized the 3D ice distribution inside the GDL after several cold-start conditions using X-ray CT. Kim et al. [40] used X-ray tomography in visualizing the GDL structure's deformation after freezing the pre-saturated GDL. Mayrhuber et al. [41] investigated the mechanism of the performance drop during the PEM fuel cell cold-start by in-situ visualization of the water production and transfer via synchrotron X-ray CT. Kim et al. [33,34] quantitively measured the heterogeneous distribution of the GDLs porosity, as well as reconstructed the 3D structure from the X-ray CT images of the GDLs after the freeze/thaw cycles. They investigated physical damage on the GDL material and structure such as irreversible porosity changes.

For GDL water management at normal and at subzero operating temperatures during cold-start, there are still many gaps to fill in order to have a clear understanding of the water transfer phenomenon. Most of the existing visualization research about the GDL water behavior were performed with a fuel cell in an idle state, where the total exposure time could take several minutes. Monochromatic beam with lower beam energy can provide a better result in spatial resolution and material contrast, but it is too slow to capture the dynamic water transfer. Limited

by the apparatus, the studies on the dynamic process often only captured 2D or low resolution 3D data. It becomes more challenging in experimental design when involving the subzero temperature condition, where the scanning time could be highly sensitive. Therefore, the dynamic freezing, thawing and water transfer processes in the cold-start GDL are not well explained. Continuing the research performed by Battrell et al. [37] at ambient conditions, the cold-start condition was applied in this experiment. The saturated GDLs were initially frozen to simulate residual ice at the subzero temperature. Although this condition was not generated through active fuel cell cold-start operation, it could still simulate the rapid ice formation with the liquid water heterogeneously produced across the domain. This could be caused by non-homogenous current distribution throughout the catalyst layer, typically with high current density and poor cold-start management [42]. Furthermore, the experiment considered multiple GDL samples (Sigracet® 35AA and 35BA graphite GDLs) and air purging rates (10, 20, 30, 50 ml/min). New X-ray detector and noise removal methods were used to improve the image resolution and data process. These dynamic GDL thawing and desaturation processes with a serpentine flow channel and 16 mm diameter GDL were captured with high speed synchrotron X-ray CT. The high-resolution images were further processed and analyzed both through the entire GDL domain and in a smaller region of interest. Realtime colormaps and 3D models were also constructed to demonstrate the localized water behavior. This research provides valuable information for future experiments and numerical simulations on the GDL water transfer and the freezing/thawing process.

3.3 Methodology

The experiments were designed based on the study by Battrell et al. [37] with several improvements and modifications on experimental conditions to fulfill the research objectives. These modifications on equipment, procedures, and image processing also increased the quality of the data analysis. Tests considered the Sigracet® 35AA and 35BA carbon fiber GDLs, which are the same series of GDL products and shared the same design and process methods with similarity in porosity (88.4 % and 89.0 %, respectively), and the GDL thickness is slightly increased from 255 μm to 280 μm [44]. The key difference is hydrophobicity, where 35BA GDLs have an additional 5% polytetrafluoroethylene (PTFE) loading compared with 35AA GDLs, resulting in higher hydrophobicity level [44,45].

For each trial of experiment, the 16 mm diameter dry state GDL sample was first assembled into a backup test cell. In this cell, the GDL was injected with 0.05 ml/min liquid water flow from the water channel by a syringe pump (NE-1000, New Era Pump Systems Inc.) [43] for 3 minutes at ambient temperature. The sample GDL was saturated as the water flowed through the GDL to the gas channel. By saturating the GDLs outside the test cell, it minimized ice blockage in the tubes and channels of the test cell caused by residual water. The saturated GDL was then transferred into the test cell, and a CT scan was performed on the GDL area to establish the initial GDL saturation. The residual water in the GDL was then frozen by placing the test cell in a -80 °C freezer for 20 minutes, which simulated the frozen PEM fuel cell GDL before the cold-start post-shutdown phase. Then the test cell, with frozen GDL inside, was quickly mounted on the CT rotation stage, and the air inlet/outlet lines were connected to the test cell at ambient temperature (22 °C) and dry conditions (0 % humidity). Flow from the compressed air tank was set at 10 ml/min, 20 ml/min, 30 ml/min and 50 ml/min depending on the experimental conditions, corresponding to 2.88 m/s, 4.26 m/s, 5.98 m/s and 9.02 m/s superficial gas velocity in the gas channel. Once the air was flowing, CT scans were performed in 2 minutes intervals for a total of 30 minutes in order to capture the dynamic water transfer during the GDL thawing process. This continuous air purge was designed for two purposes: 1. To simulate dry gas purging in the cold-start protocols; 2. Increase the speed of liquid water removal compared to evaporation. After the continuous CT scans, a 5 minute air purge at 100 ml/min was applied to the GDL to reach the dry state, and an X-ray CT was captured of this dry GDL as the baseline. In each experiment trial, the sample GDL remained in the test cell untouched as soon as the cell was assembled to minimize the position change of the captured images during the scan. The assembled cell on the X-ray stage is shown in Figure 3.1-A.

3.3.1 Test cell design and setup

The test cell used in this experiment simulated the cathode side of a single PEM fuel cell unit. The disassembled test cell is shown in Figure 3.1-B, where the sample GDL, shown in Figure 3.1-C, was placed between the gas and water channels when assembled. The edge of the GDL-channel area was sealed with gaskets. The gas and water channels, shown in Figure 3.1-D, were identical, each 40 mm length in serpentine shape, with 1 mm (w) x 0.5 mm (h) cross sectional area. Polyether ether ketone (PEEK) was selected as the cell material for its high durability and low X-ray absorption rate (X-ray mass attenuation coefficients = 0.509 cm^2/g),

and the total available X-ray for scanning was 54.6 % of the original energy after it penetrated the cell walls. During the experiment, the inlet/outlet of the water channel were sealed, which forced the purging air to flow along the gas channel.

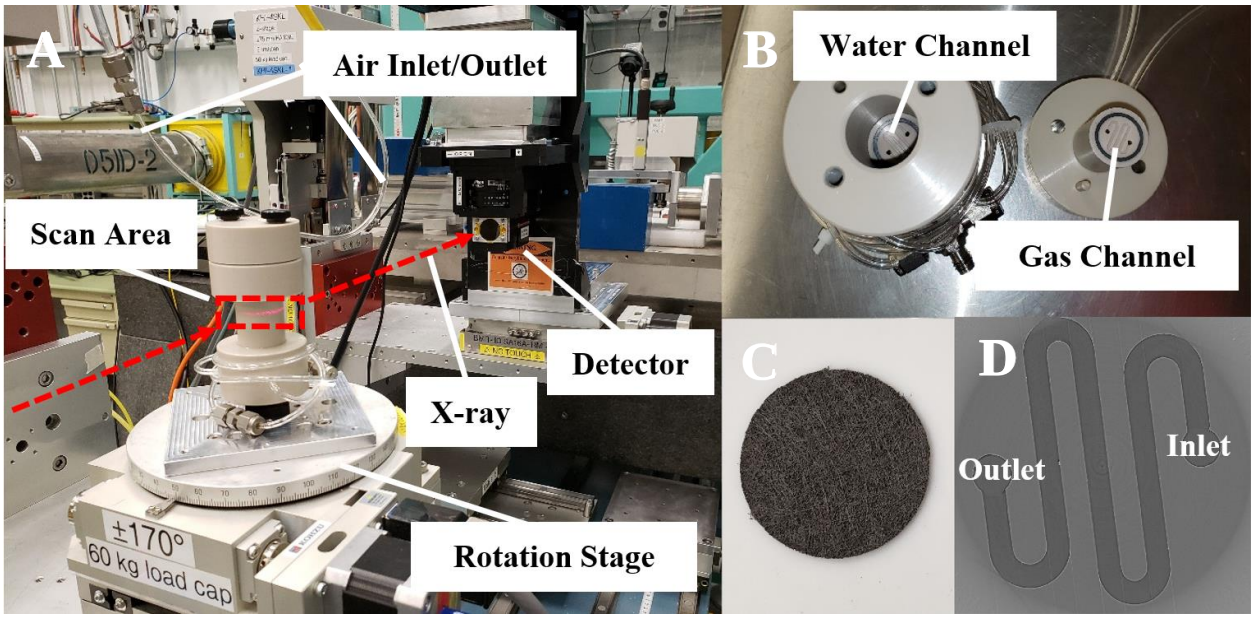

Figure 3.1. A) Experimental setup in X-ray scanning chamber, with the test cell mounted on the rotation stage and air tubes connected; the scan area and the beam path were highlight in red. B) disassembled test cell displaying the water channel and the gas channel. C) Sample GDL used in experiments, cropped in 16 mm diameter. D) Reconstructed X-ray CT image demonstrating gas channel with air inlet and outlet labeled.

3.3.2 Synchrotron and CT setup

All the experiments for this research were performed at the Bio-Medical Imaging and Therapy (BMIT) 05B1-1 beamline in the Canadian Light Source Inc., the 3rd generation synchrotron facility located in Saskatoon, Canada [46]. The filtered polychromatic beam with high photon flux made it possible for the high resolution and high-speed CT, which was able to capture the dynamic water movement inside the GDLs with minimized motion artifacts in each scan. 2000 projections were captured in 10 seconds during each CT scan using a detector (a high speed camera DIMAX HS4 (PCO) combined with a beamline monitor AA40 (HAMAMATSU)) with the pixel size of 5.3 µm, and a Field of View (FOV) of 10 mm x 1.5 mm. The small FOV set reduces the readout time and enables the test to cover the entire GDL area in the vertical direction. The detector was placed 0.4 m from the cell to enhance the phase contrast of the

images, where the scan area and path of the X-ray are highlighted in Figure 3.1-A. The test cell was immobilized on the rotation stage with a strong magnetic mount, and the stage was controlled to return to the same position before each CT scan to keep consistency of the GDL orientation in the images at different time points.

3.3.3 Image processing and calculation

Raw 2D projection images from the CT scan were first reconstructed with ultra-fast imaging and online reconstruction - Karlsruhe Institute of Technology (UFO-KIT) [47, 48]. Background correction was performed using dark-field and flat-field images to remove artifacts which might be introduced from the filter and detector. Phase retrieval, with delta/beta ratio = 50, was applied along with the reconstruction for the phase contrast imaging method. It can also reduce noise from the oscillation of the polychromatic beam. Figure 3.2-A shows a slice of the 32-bit black-and-white reconstructed image, where the brighter color represents the GDL structure (carbon fiber), water and ice, and the darker color represents unoccupied space (air). The same image format was used for all the later processing and calculation. These reconstructed CT images were then imported into ImageJ 1.52a for segmentation and calculation. Outlier removal was applied by slightly calibrating the images using the reported porosity value for the GDL product while not over-modified to damage the image quality. The GDL material and the water/ice mixture were identified by tuning the threshold on the grayscale. Figure 3.2-B shows a slice of image with the threshold on the grayscale set to -7.00×10^4, where all the non-vacant area is segmented and highlighted in red. As the histogram of the image shows in Figure 3.2-C, the regions of the carbon fiber/water/ice on the grayscale overlapped (highlighted in red box), especially for the water/ice due to insignificant density difference. With the images from the high-speed polychromatic beam X-ray CT, it is difficult to identify the carbon fiber/water/ice from each other only via the image contrast. Therefore, the liquid water/ice mixture in each CT scan was distinguished from the carbon fiber by subtracting the fiber structure in the images of the dry state GDL from the images of the wet GDL. A smaller circular area compared to Field of View shown in Figure 3.2-B, centered with the channel location, was used for further calculation to avoid the truncation artifacts along the edge of the image. The percentage-saturation of the GDL was calculated as the water/ice mixture volume divided by the total pore volume in the dry state GDL. The desaturation rate of the GDL was calculated as the change in the mass of

water/ice mixture over 4 minutes divided by cross sectional area of the GDL. Avizo 9.3 was used for 3D visualization of the localized liquid water/ice transferring in the GDLs.

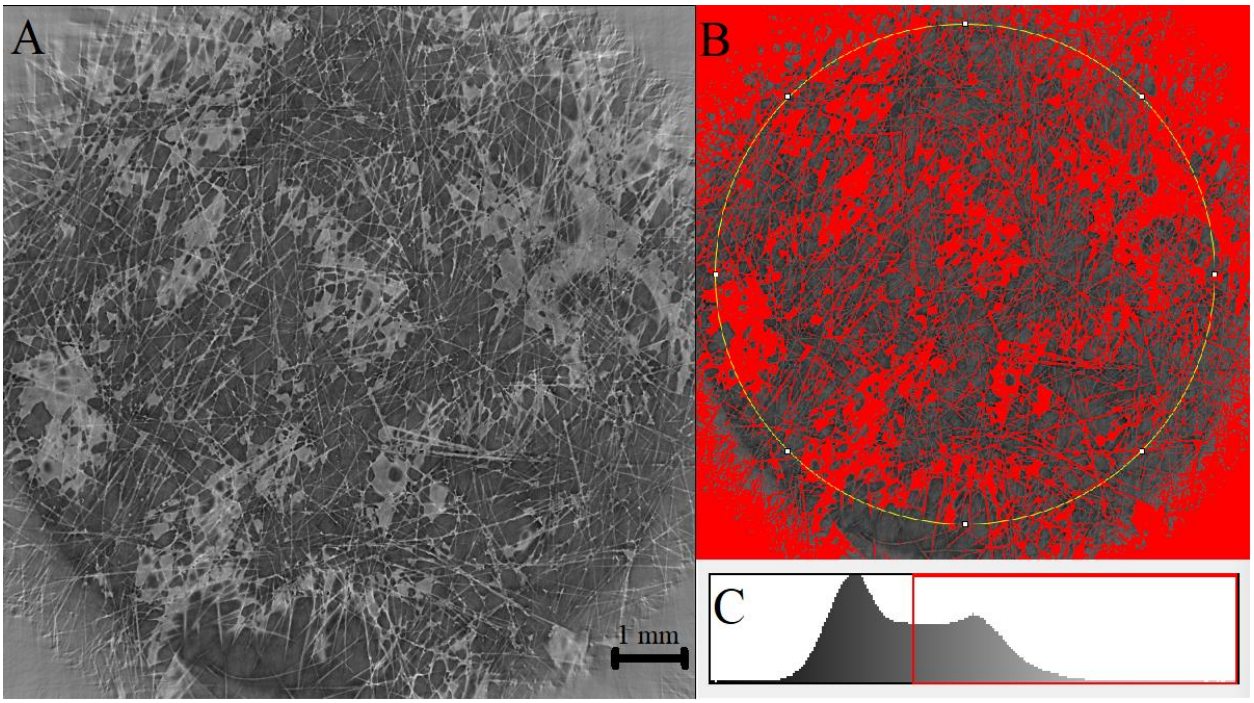

Figure 3.2. A slice of reconstructed CT image from 35AA GDL with 20 ml/min air purging rate at 10 minutes. A) Reconstructed image. B) Segmented with selected threshold. C) Histogram of the grayscale.

3.4 Results and discussion

3.4.1 Saturation profile and desaturation rate over the entire GDL domain – effects of the air purging rate and GDL hydrophobicity

Sixteen CT scans were captured for each trial to cover the 30 minutes thawing and desaturation process, with the air purging rate set to 10, 20, and 30 ml/min, corresponding to 2.88 m/s, 4.26 m/s and 5.98 m/s superficial gas velocity. For the trial with 50 ml/min air purging rate (9.02 m/s superficial gas velocity), only 15 minutes were captured due to the higher rate of change of the water content. The experiments were performed in the incremental order of the air purging rates and were performed on the same GDL sample as the experiments progressed.

Based on the collected CT images, the dynamic saturation profile over the entire GDL domain was analyzed for each experimental trial to study the effects of the air purging rate, shown in Figure 3.3-A and B. By comparing the plots, the saturation profiles of all the experimental cases share a similar trend. Initially, the curves were almost flat from 0 to 10

minutes, corresponding to ice thawing. Then, the saturation decreased, meaning water was removed from the GDL. Finally, the curves started to flatten again at approximately 20 to 30 minutes. The initial saturation of each trial increased as the experiments proceeded, though the procedures and the GDL sample were identical through the experiments. For example, the initial saturation for the 35AA experiments increased from 6.04%, to 11.9%, and then 16.2% for the cases of 10, 20, and 30 ml/min air purging rates, as more experiments had been done to the same GDL sample. To verify this observation, few experiments were performed using a brand new 35AA GDL sample with the air purging rates in a decremental order. The initial saturation increased from 3.99 % to 11.9 % for the cases of 30 and 10 ml/min air purging rates. No significant porosity difference was found from the GDL samples after each trial, as the overall porosity of the dry GDL in the cases of 10, 20, and 30 ml/min air purging rates only had a 1.16 % difference and no trend in porosity change was noted as a function of the flow rate. This difference in initial saturation could occur possibly due to the GDL experiencing irreversible damage during the rapid freezing and water injection, which may include fiber cracking and minor GDL structure deformation without considerable porosity changes.

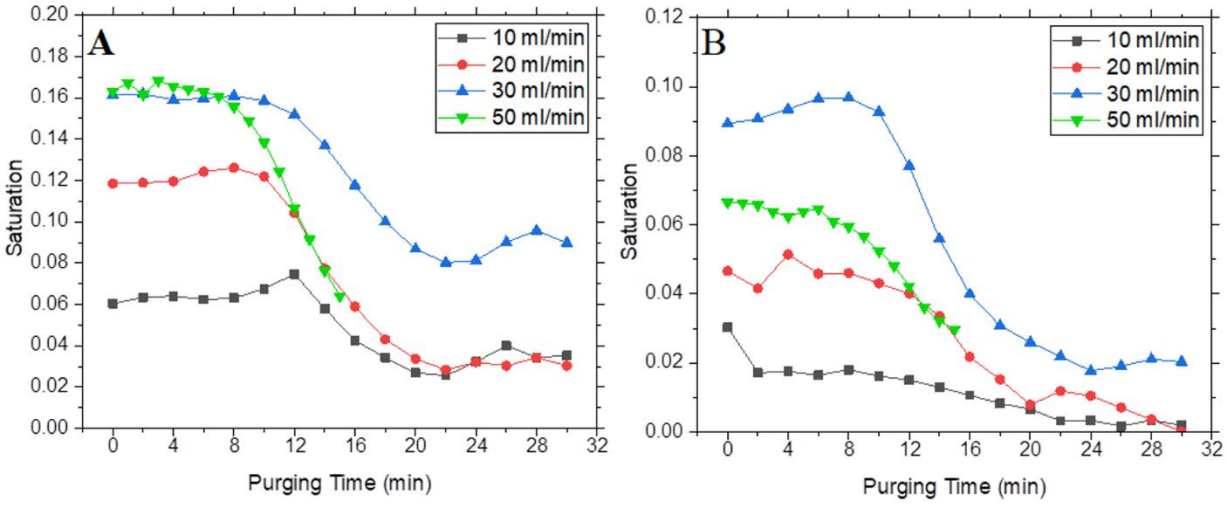

Figure 3.3. Dynamic saturation profiles for A) 35AA GDL, B) 35BA GDL over the entire GDL domain, with 10, 20, 30, and 50 ml/min air purging rates.

The average desaturation rates over the purging process are shown in Table 3.1. Battrell et al. [37] reported 0.0030 µL cm^{-2} s^{-1} as the overall desaturation rate with a 35AA GDL with 50 ml/min air purging rate. Despite similar cell geometry and procedures, that work did not include

the freezing and thawing, thus the average desaturation rates in this experiment were similar but lower in magnitude.

Table 3.1. Average desaturation rate for the whole purging process over the entire GDL domain

		10 ml/min	20 ml/min	30 ml/min	50 ml/min
Desaturation rate (μL cm^{-2} s^{-1})	35AA	0.000173	0.000563	0.000425	0.00121
	35BA	0.000198	0.000377	0.000606	0.000593

The desaturation rates were also analyzed for the entire GDL domain based on the same experimental data, shown in Figure 3.4-A and B, where the desaturation flux was calculated in the average of 4 minutes. These plots exhibit similar behavior to the dynamic saturation profiles. The desaturation rates were close to 0 μL cm^{-2} s^{-1} for the first 5-10 minutes, where the temperature of the GDL increased via convection but did not reach the melting point. In the next phase, water thawing and removal occurred in the GDL. The water removal rate increased as more water transformed into the liquid phase, which corresponded to the increase of the desaturation rate from approximately 5 to 15 minutes. As the desaturation rate reached the peak, for 35AA GDL with 50 ml/min, the desaturation rate is similar to the liquid water removal rate reported by Battrell et al. [37], which indicated that the GDL was completely thawed at this moment. For the rest of the purging process, the desaturation rate decreased to 0 μL cm^{-2} s^{-1} where most of the water content was removed from the GDL. In the last phase, the desaturation rate fluctuated around 0 μL cm^{-2} s^{-1}. For comparison, the overall GDL desaturation plot on 35AA GDL with 50 ml/min air purging rate from Battrell et al. is shown in Figure 3.5, where the experiment was performed at ambient temperature. Without the cold-start condition involved, the desaturation rate is a non-zero value at the beginning of the purging process. For the first 15 minutes, the desaturation for the ambient temperature GDL was approximately linear at 0.0018 μL cm^{-2} s^{-1}, which is different from the increasing desaturation for the frozen GDL. The negative desaturation rates observed during the purging process with cold-start condition indicated that water may enter the GDL system. Due to the through-plane pressure difference caused by the purge flow, a small amount of water from the droplets and water films attached to the bottom surface of the GDL could be sucked into the GDL porous network. This liquid water was then quickly removed with the purging air, causing the sudden increase in the desaturation rates.

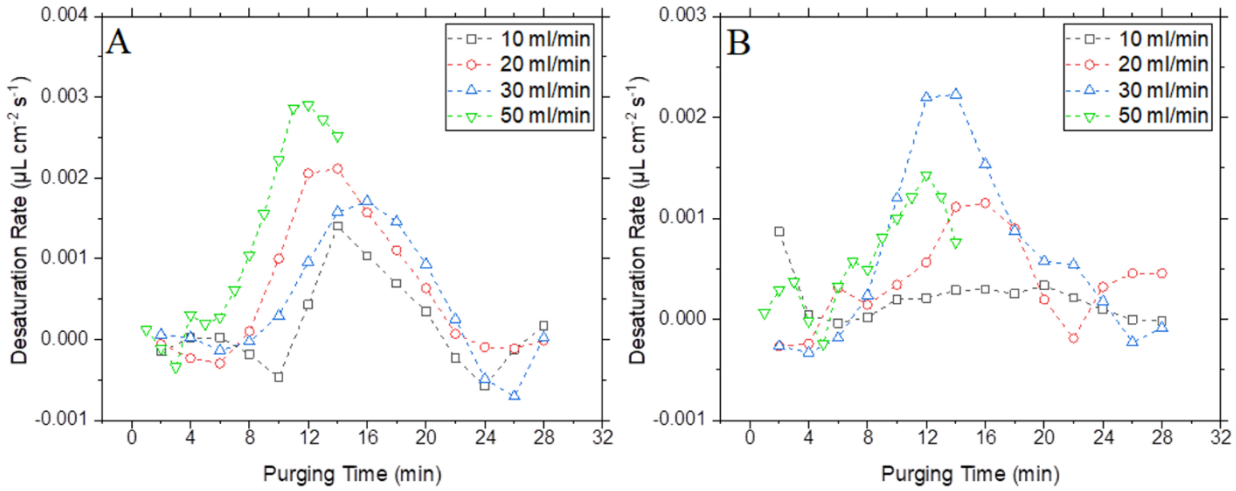

Figure 3.4. Dynamic desaturation profiles for A) 35AA GDL, B) 35BA GDL over the entire GDL domain, with 10, 20, 30, and 50 ml/min air purging rates.

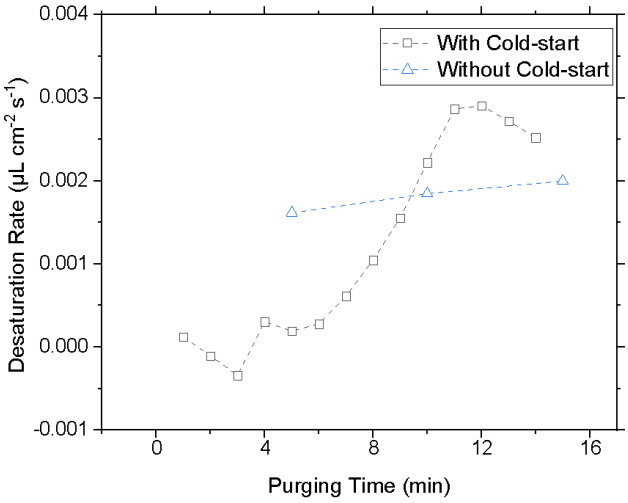

Figure 3.5. Comparison of desaturation profiles for 35AA GDL with 50 ml/min air purging rate, with or without the cold-start conditions (data for the desaturation profiles without the cold-start conditions was presented by Battrell et al. [37])

The average desaturation rates for the whole purging process shown in Table 1, and the peak desaturation rates shown in Figure 3.4, generally increase with higher air purging rates. Also, the lengths of the first two phases, which are the warmup and the thawing/water removal process, generally decrease with increasing flow rate and shift to the left on the desaturation plots shown in Figure 3.4. These results indicate that in the large scale of the GDL domain, the thawing and desaturation processes speed up as the air purging rate increases. Two outliers,

35AA with 30 ml/min and 35BA with 50 ml/min air purging rate, were detected during the analysis from the lower than expected average desaturation rates and the abnormal desaturation profiles. The cause of these outliers, strong heterogenous behavior in the GDL desaturation, is discussed in Section 3.4.3.

In studying the effects of the GDL hydrophobicity, the 35BA GDL was tested with the same air purging rates. The 35BA GDL has 5 % PTFE filling vs. 0 % with 35AA GDL, increasing the hydrophobicity. Data from Table 1 show no clear trends in the average desaturation rates when shifting from 35AA to 35BA GDLs. Also, the time taken in each phase of the thawing and desaturation process shown in Figure 3.4 are similar with both GDLs. It indicates that the GDL hydrophobicity has only limited effects on the overall thawing and desaturation process. However, the peak values of the desaturation profiles shown in Figure 3.4 decrease as the GDL hydrophobicity increases (excluding the outlier cases). Also, the GDL hydrophobicity shows major effects on the GDL initial saturation. The initial saturation levels increase by 3.31, 2.37, 1.77, and 1.97 times from 35BA to 35AA GDLs in the cases of 10, 20, 30, and 50 ml/min air purging.

3.4.2 In-plane heterogenous water distribution and desaturation

Based on observation and previous research, a high level of heterogeneity can occur in the saturation and desaturation process in a large scale GDL domain. Due to this heterogeneity, it is not precise to describe the level of water blockage in a GDL with the overall GDL saturation. For instance, 10 % average saturation was observed for 35AA with 20 ml/min air purging rate at 12 minutes, with 30 ml/min at 18 minutes, and with 50 ml/min with 12 minutes. However, the colormap contours and the histograms of the saturation level shown in Figure 3.6 indicate the unequal water blockage levels spatially in the three cases. These contours were constructed by segmenting the entire circular GDL field of view with 1800 pixels in diameter into a square of 25 x 25 pixels. The saturation value in each segment shown on the contour was calculated individually for all GDL slices through-plane, and the average value is presented in the 2D result here.

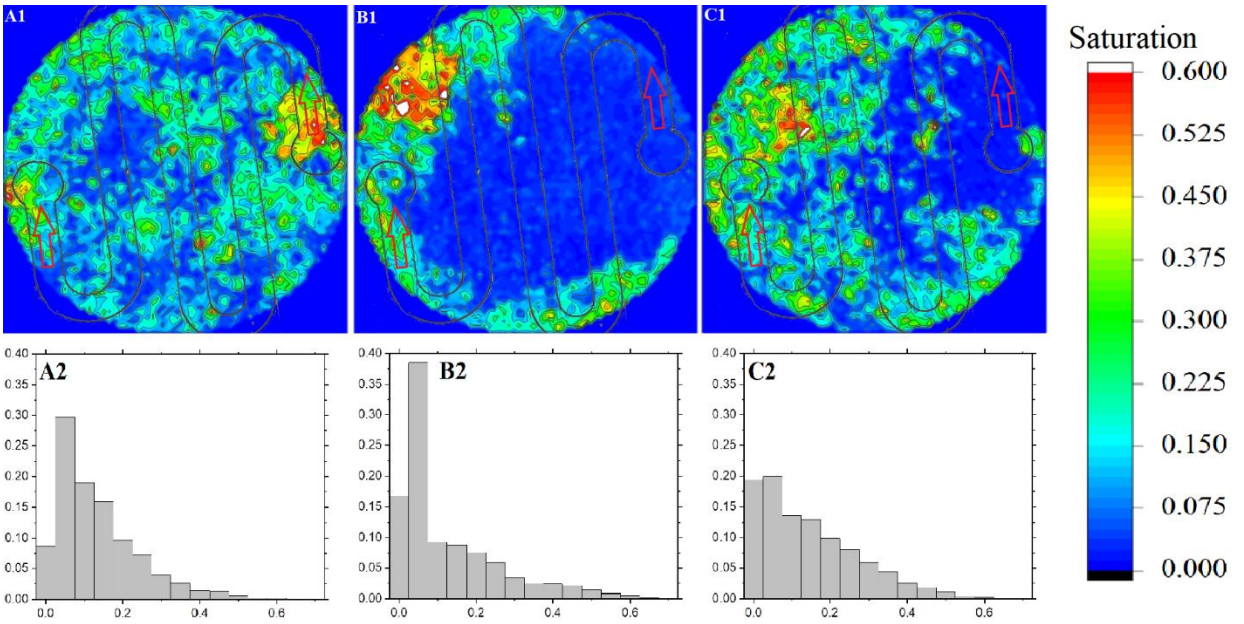

Figure 3.6. Colormaps (1) and histograms (2) based on the through-plane averaged saturation for A) 35AA GDL with 20 ml/min air purging rate at 12 minutes B) 35AA GDL with 30 ml/min air purging rate at 18 minutes C) 35AA GDL with 50 ml/min air purging rate at 12 minutes.

The water in the 20 ml/min case shown in Figure 3.6-A was widely distributed through the entire GDL domain with few higher water saturation spots. For the 50 ml/min case shown in Figure 3.6-C, the water distribution was more concentrated on the left side of the GDL, and more dry area occurred in the GDL compared to the 20 ml/min case. For the 30 ml/min case shown in Figure 3.6-B, water accumulated in a relatively small GDL area with few highly concentrated water spots. Thus, despite the same total saturation, the impact of the local saturation on PEM fuel cell behavior could be different in each case.

For the large scale of the GDL domain, the water blockage level of the 20 ml/min case was the highest among the 3 cases, with 38.3 % of the GDL area dry where the saturation was lower than 1 %. The 30 ml/min case was the lowest in the general water blockage level with 55.3 % of the GDL area dry, but it had the highest regional water blockage level, where the highest saturation in the water-concentrated spot was 66.0 %. Thus, it would be inaccurate to describe the water blockage level only in the terms of the overall GDL saturation. This is particularly true of continuum models that treat the porous media as one with homogenous properties, and the data here can serve as validation for local models such as done via pore

network models. Other parameters such as localized saturation and the distribution of the saturation should to be considered in future experimental and modeling studies.

3.4.3 Localized saturation profile and desaturation rate – regional water accumulation

As previously mentioned, two experimental cases, 35AA with 30 ml/min air purging rate and 35BA with 50 ml/min air purging rate, experienced lower overall desaturation than expected. For 35AA with 30 ml/min air purging rate, the colormap contours of the GDL desaturation process, using the same approach in Figure 3.6, are shown in Figure 3.7. A water accumulation region was found, which represents approximately 10 % of the GDL area, located at the upper-left corner of the image above the air outlet. In this region, the desaturation rate of the GDL was negative through the entire purging process, indicating accumulation of water. The saturation level persistently increased to above 60 % for most of the region at 24 minutes.

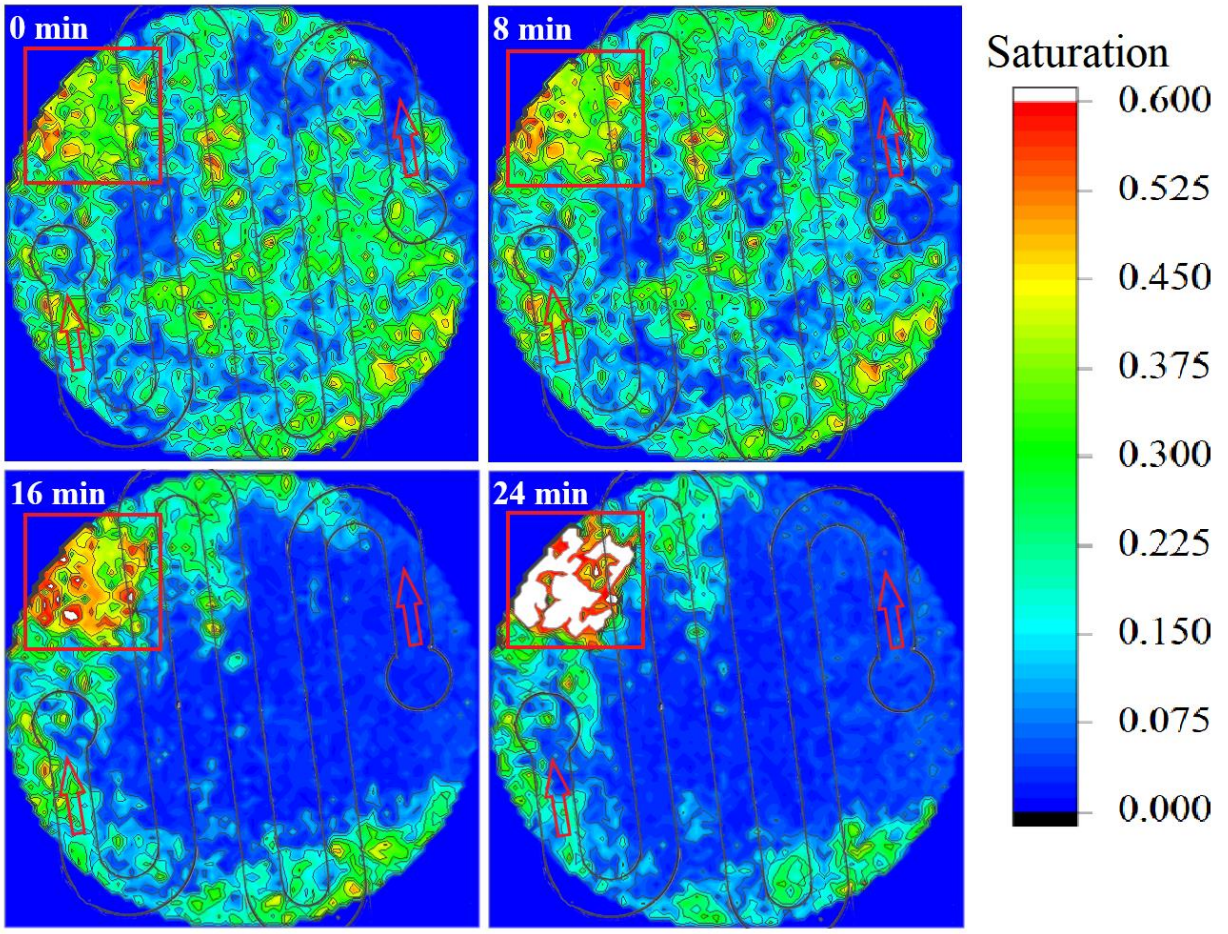

Figure 3.7. Colormaps based on the through-plane averaged saturation of the desaturation process at 0, 8, 16, and 24 minutes for 35AA GDL with 30 ml/min air purging rate, with the channel location, the air purging direction, and the water accumulation region.

For this case, the desaturation rate for the overall GDL, the water accumulation region, and the other region are shown in Figure 3.8. The other region refers to the GDL area not in the water accumulation region. By deselecting the water accumulation region in the calculation, the average desaturation rate of the other GDL region increased from 0.000425 μL cm^{-2} s^{-1} to 0.000526 μL cm^{-2} s^{-1}, and the peak desaturation rate increased from 0.00171 μL cm^{-2} s^{-1} to 0.00193 μL cm^{-2} s^{-1}. The saturation level in the water accumulation region increased steadily from 0 to 18 minutes, and experienced fluctuations in the desaturation rate from 20 to 30 minutes.

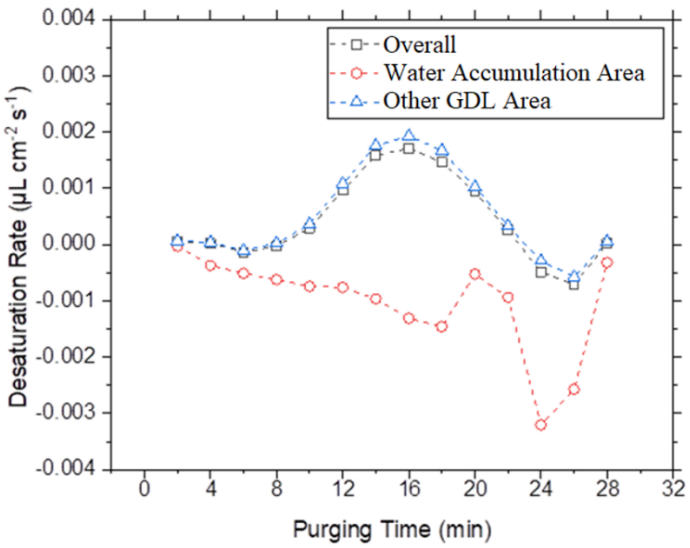

Figure 3.8. Dynamic desaturation rate profiles for 35AA GDL with 30 ml/min air purging rate, which included the desaturation rate of the entire GDL domain, slow desaturation region, and the GDL area besides the slow desaturation region.

The negative desaturation values and an increase in the saturation in the colormaps indicate that water was introduced and concentrated into this area instead of being purged out. This concentrating behavior of the water content was also found in other cases, but the area of the concentrated water spots was smaller and occurred in various regions. The purging could be inefficient in this dead zone, and water from the nearby region might be brought into this area via the air flow. Also, the volume expansion of the water content was counted in the saturation change as it transformed from ice into liquid. Assuming no water removal from the water accumulation region in 35AA 30 ml/min case, the volume expansion from ice melting could account for 26.5 % of the total saturation increase from 0 to 24 minutes.

3.4.4 Localized saturation profile – through-plane heterogenous behavior

The heterogenous behavior of the water saturation and desaturation happens not only in-plane, but also occurs through-plane in the GDL. For this analysis, the GDLs were evenly divided into the top, middle, and bottom sections vertically. Each section was 53.0 μm and 68.9 μm in height for the 35AA and 35BA GDLs, respectively. The dynamic saturation profile and desaturation rate of the 35AA GDL at 20 ml/min air purging rate are shown in Figure 3.9-A and B as examples. In terms of initial saturation, water tended to reside in the top and bottom GDL sections, where the middle GDL section contained a minimum level of saturation. Counting all

the experimental cases, the average initial saturation level of the top, middle, and bottom GDL section for the 35AA GDL was 24.5 %, 2.97 %, and 17.9 %, respectively. This result occurred even though injected water was forced to flow through the GDL from bottom to top in the initial saturation process. In terms of desaturation rate, the trend was not clear since other factors rather than the spatial parameter in the vertical direction such as GDL geometric location, initial water saturation, and GDL boundary condition may all play significant roles in the desaturation process.

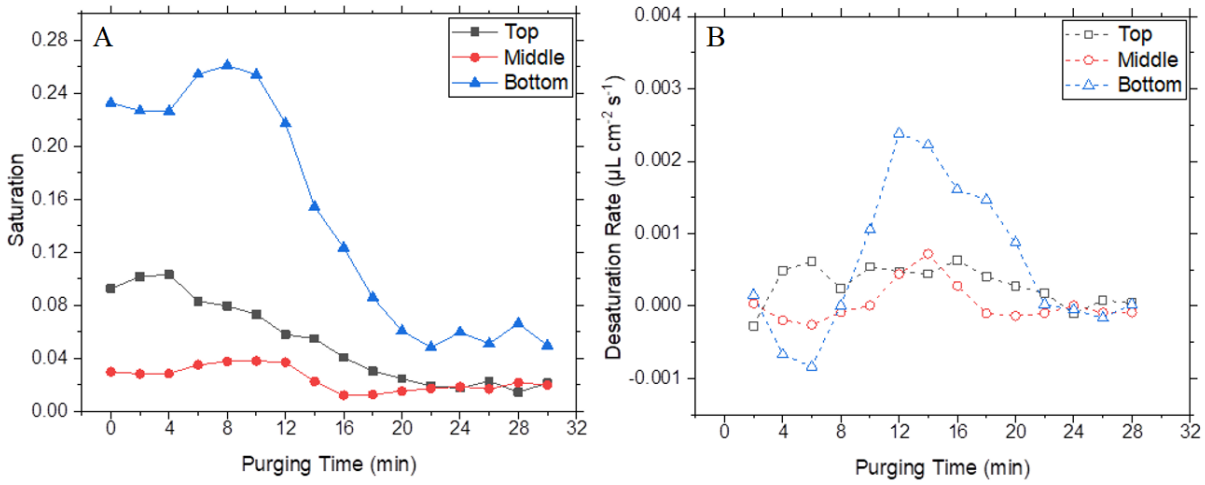

Figure 3.9. A) Dynamic saturation profiles and B) desaturation rate profiles of top, middle, and bottom 35AA GDL sections with 20 ml/min air purging rate.

When focusing on the water behavior in a localized area, additional information can be seen in the example shown in Figure 3.10. CT images of the GDL central area from the case of 35AA 20 ml/min were processed into 3D models via Avizo 9.3. The 600 x 600 pixels (3.18 x 3.18 mm) square highlighted in Figure 3.10-A covers the area of the center of the middle channel and two ribs beside it. The GDL fiber and the liquid water/ice mixture were segmented and reconstructed into grey and light blue, respectively. For easier demonstration, the top half of the GDL fiber structures were hidden in the 3D models, and the red lines were added onto the models to represent the boundary of the channel and rib. From 0 to 8 minutes, no significant water transfer was found in this region. From 8 to 16 minutes, the majority of the water content located at the top half of the GDL under the right rib was removed, and the water in the other region remained relatively stationary. From 16 to 24 minutes, all other water content was

removed except at the bottom half of the GDL under the left rib. It shows that the channel and GDL geometry play important roles in the desaturation, where the GDL under the channel and rib, or even under two different ribs, could be significantly different in the desaturation behavior. In terms of the vertical direction, water content seems to be removed from the top half of the GDL first then the bottom part.

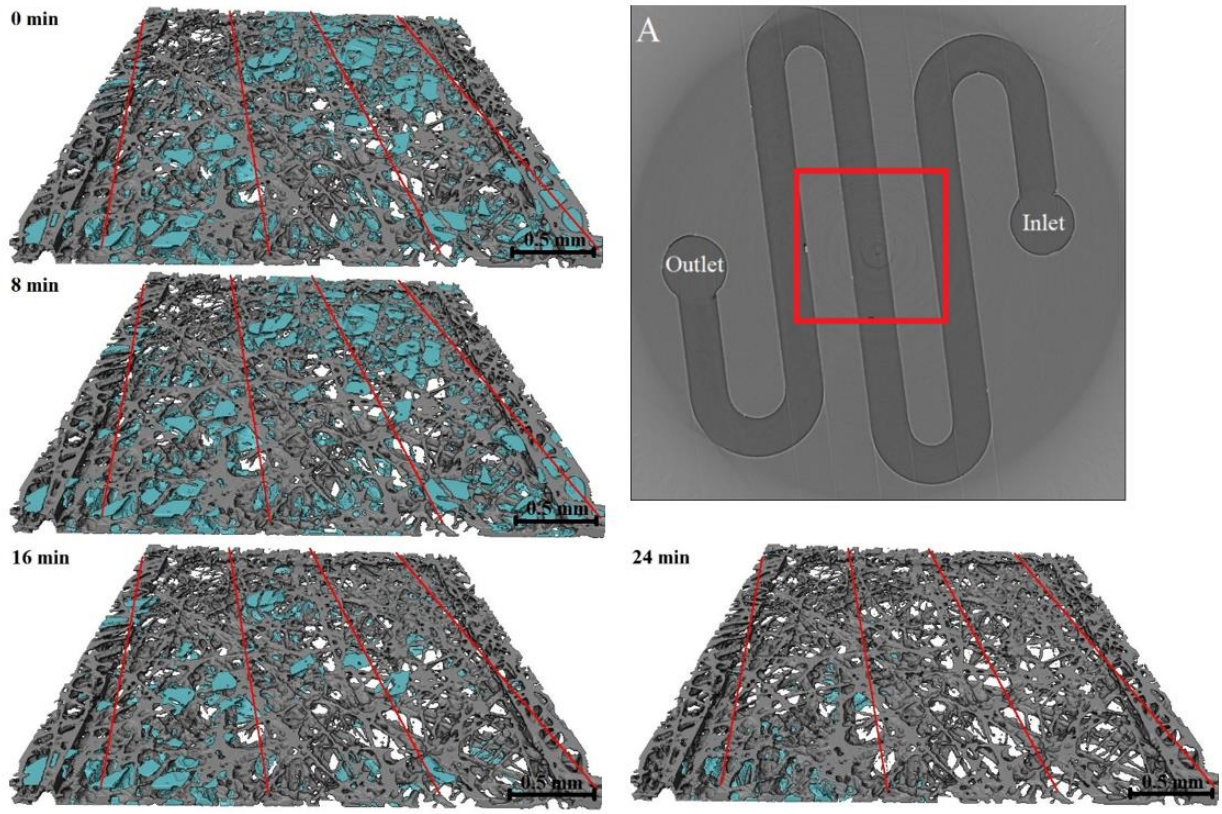

Figure 3.10. Localized 3D models of the thawing and desaturation process with channel location for 35AA GDL with 20 ml/min air purging rate at 0, 8, 16, 24 minutes, with indication of A) data selection area.

3.5 Conclusion

Visualization and quantification of the thawing and desaturation process with dry air purging on frozen, initially saturated GDLs was performed using high speed, high resolution synchrotron X-ray CT. Data analysis was performed based on the CT images, focusing on the dynamic saturation profile and desaturation rates. In the large scale of the entire GDL area, similar trends were found for the desaturation process through all the experimental cases, which

considered air flow rate and GDL hydrophobicity. These trends included an initial thawing process, desaturation where water was removed from the GDL, and a final steady state water profile. The air purging rate has a major effect on the thawing and desaturation process, while the hydrophobicity of the GDL affects mainly the GDL initial saturation. Zooming in a smaller GDL area, heterogeneity was observed through the entire GDL domain. Data from segmentation (saturation contours and histograms) and localized 3D models show that the level of water blockage in a GDL locally can vary substantially, indicated that the GDL cannot be precisely characterized by the overall saturation value alone. Heterogenous behaviors, such as water accumulation spots and uneven desaturated GDL layers, were observed in-plane and through-plane of the GDLs, affecting desaturation rates. These results expand the knowledge of the water transfer behaviors during the cold-start thawing process, and show the complexity in fully understanding the GDL water management. The heterogeneity of the GDL water behavior needs to be considered in future experimental and modeling works, as well as in the commercial PEM fuel cell design.

3.6 Acknowledgements

LFZ and RA acknowledge the support from their respective universities, the University of Saskatchewan and Montana State University. LFZ also acknowledges financial support from Natural Sciences and Engineering Research Council of Canada. Experiments and image processing described in this paper were performed at the BMIT facility at the Canadian Light Source, which is supported by the Canada Foundation for Innovation, Natural Sciences and Engineering Research Council of Canada, the University of Saskatchewan, the Government of Saskatchewan, Western Economic Diversification Canada, the National Research Council Canada, and the Canadian Institutes of Health Research.

3.7 References

[1] Spiegel, Colleen. *PEM Fuel Cell Modeling and Simulation Using Matlab*. Burlington: Elsevier Science, 2011.

[2] Hardman, Scott, Robert Steinberger-Wilckens, and Dan van der Horst. “Disruptive Innovations: The Case for Hydrogen Fuel Cells and Battery Electric Vehicles.”

International Journal of Hydrogen Energy 38, no. 35 (2013): 15438–51. https://doi.org/10.1016/j.ijhydene.2013.09.088.

[3] Anderson, Ryan, Lifeng Zhang, Yulong Ding, Mauricio Blanco, Xiaotao Bi, and David P. Wilkinson. "A Critical Review of Two-Phase Flow in Gas Flow Channels of Proton Exchange Membrane Fuel Cells." *Journal of Power Sources* 195, no. 15 (2010): 4531–53. https://doi.org/10.1016/j.jpowsour.2009.12.123.

[4] Andersson, M., S.B. Beale, M. Espinoza, Z. Wu, and W. Lehnert. "A Review of Cell-Scale Multiphase Flow Modeling, Including Water Management, in Polymer Electrolyte Fuel Cells." *Applied Energy* 180 (2016): 757–78. https://doi.org/10.1016/j.apenergy.2016.08.010.

[5] Amamou, Ali Akrem, Sousso Kelouwani, Loic Boulon, and Kodjo Agbossou. "A Comprehensive Review of Solutions and Strategies for Cold Start of Automotive Proton Exchange Membrane Fuel Cells." *IEEE Access* 4 (2016): 4989–5002. https://doi.org/10.1109/access.2016.2597058.

[6] Lin, Rui, Yuanming Weng, Xuwei Lin, and Feng Xiong. "Rapid Cold Start of Proton Exchange Membrane Fuel Cells by the Printed Circuit Board Technology." *International Journal of Hydrogen Energy* 39, no. 32 (2014): 18369–78. https://doi.org/10.1016/j.ijhydene.2014.09.065.

[7] Siegwart, M., F. Huang, M. Cochet, T. J. Schmidt, J. Zhang, and P. Boillat. "Spatially Resolved Analysis of Freezing during Isothermal PEFC Cold Starts with Time-of-Flight Neutron Imaging." *Journal of The Electrochemical Society* 167, no. 6 (2020): 064510. https://doi.org/10.1149/1945-7111/ab7d91.

[8] Kim, Seung-Gon, and Sang-Joon Lee. "A Review on Experimental Evaluation of Water Management in a Polymer Electrolyte Fuel Cell Using X-Ray Imaging Technique." *Journal of Power Sources* 230 (2013): 101–8. https://doi.org/10.1016/j.jpowsour.2012.12.030.

[9] Luo, Yueqi, Qian Guo, Qing Du, Yan Yin, and Kui Jiao. “Analysis of Cold Start Processes in Proton Exchange Membrane Fuel Cell Stacks.” *Journal of Power Sources* 224 (2013): 99–114. https://doi.org/10.1016/j.jpowsour.2012.09.089.

[10] Ko, D., S. Doh, D. I. Yu, H. S. Park, and M. H. Kim. “The Change of Water Distribution in Porous Media of the Polymer Electrolyte Membrane Fuel Cell after Freeze/Thaw Cycles.” *Fuel Cells* 18, no. 4 (2018): 413–21. https://doi.org/10.1002/fuce.201700121.

[11] Hwang, Gi Suk, Hyoungchul Kim, Roger Lujan, Rangachary Mukundan, Dusan Spernjak, Rodney L. Borup, Massoud Kaviany, Moo Hwan Kim, and Adam Z. Weber. “Phase-Change-Related Degradation of Catalyst Layers in Proton-Exchange-Membrane Fuel Cells.” *Electrochimica Acta* 95 (2013): 29–37. https://doi.org/10.1016/j.electacta.2013.02.017.

[12] Schmittinger, Wolfgang, and Ardalan Vahidi. “A Review of the Main Parameters Influencing Long-Term Performance and Durability of PEM Fuel Cells.” *Journal of Power Sources* 180, no. 1 (2008): 1–14. https://doi.org/10.1016/j.jpowsour.2008.01.070.

[13] Kim, S., and M.M. Mench. “Physical Degradation of Membrane Electrode Assemblies Undergoing Freeze/Thaw Cycling: Micro-Structure Effects.” *Journal of Power Sources* 174, no. 1 (2007): 206–20. https://doi.org/10.1016/j.jpowsour.2007.08.111.

[14] Chen, Huicui, Xin Zhao, Tong Zhang, and Pucheng Pei. “The Reactant Starvation of the Proton Exchange Membrane Fuel Cells for Vehicular Applications: A Review.” *Energy Conversion and Management* 182 (2019): 282–98. https://doi.org/10.1016/j.enconman.2018.12.049.

[15] Li, Pengcheng, Pucheng Fei, Yongling He, and Xing Yuan. “A Starvation Diagnosis Method for a PEM Fuel Cell during Dynamic Loading.” *Gaojishu Tongxin/Chinese High Technology Letters* 23, no. 2 (2013): 189–95. https://doi.org/10.3772/j.issn.1002-0470.2013.02.012.

[16] Liang, Dong, Qiang Shen, Ming Hou, Zhigang Shao, and Baolian Yi. “Study of the Cell Reversal Process of Large Area Proton Exchange Membrane Fuel Cells under Fuel Starvation.” *Journal of Power Sources* 194, no. 2 (2009): 847–53. https://doi.org/10.1016/j.jpowsour.2009.06.059.

[17] Taniguchi, Akira, Tomoki Akita, Kazuaki Yasuda, and Yoshinori Miyazaki. “Analysis of Electrocatalyst Degradation in PEMFC Caused by Cell Reversal during Fuel Starvation.” *Journal of Power Sources* 130, no. 1-2 (2004): 42–49. https://doi.org/10.1016/j.jpowsour.2003.12.035.

[18] Knights, Shanna D, Kevin M Colbow, Jean St-Pierre, and David P Wilkinson. “Aging Mechanisms and Lifetime of PEFC and DMFC.” *Journal of Power Sources* 127, no. 1-2 (2004): 127–34. https://doi.org/10.1016/j.jpowsour.2003.09.033.

[19] Guo, Qian, Yueqi Luo, and Kui Jiao. “Modeling of Assisted Cold Start Processes with Anode Catalytic Hydrogen–Oxygen Reaction in Proton Exchange Membrane Fuel Cell.” *International Journal of Hydrogen Energy* 38, no. 2 (2013): 1004–15. https://doi.org/10.1016/j.ijhydene.2012.10.067.

[20] Tang, Hong-Yue, Anthony D. Santamaria, John Bachman, and Jae Wan Park. “Vacuum-Assisted Drying of Polymer Electrolyte Membrane Fuel Cell.” *Applied Energy* 107 (2013): 264–70. https://doi.org/10.1016/j.apenergy.2013.01.053.

[21] Tajiri, Kazuya, Chao-Yang Wang, and Yuichiro Tabuchi. “Water Removal from a PEFC during Gas Purge.” *Electrochimica Acta* 53, no. 22 (2008): 6337–43. https://doi.org/10.1016/j.electacta.2008.04.035.

[22] Zhu, Yike, Rui Lin, Zhenghua Jiang, Di Zhong, Bohan Wang, Wangyi Shangguan, and Lihang Han. “Investigation on Cold Start of Polymer Electrolyte Membrane Fuel Cells with Different Cathode Serpentine Flow Fields.” *International Journal of Hydrogen Energy* 44, no. 14 (2019): 7505–17. https://doi.org/10.1016/j.ijhydene.2019.01.266.

[23] Li, Calvin H., and G. P. Peterson. “Experimental and Numerical Study on the Cold Start Performance of a Single PEM Fuel Cell.” *Advances in Mechanical Engineering* 2 (2010): 403816. https://doi.org/10.1155/2010/403816.

[24] BAO, C, M OUYANG, and B YI. “Analysis of the Water and Thermal Management in Proton Exchange Membrane Fuel Cell Systems.” *International Journal of Hydrogen Energy* 31, no. 8 (2006): 1040–57. https://doi.org/10.1016/j.ijhydene.2005.12.011.

[25] Oszcipok, M., M. Zedda, D. Riemann, and D. Geckeler. “Low Temperature Operation and Influence Parameters on the Cold Start Ability of Portable PEMFCs.” *Journal of Power Sources* 154, no. 2 (2006): 404–11. https://doi.org/10.1016/j.jpowsour.2005.10.035.

[26] Rajbongshi, Biju Mani, M. Shaneeth, and Anil Verma. “Investigation on Sub-Zero Start-up of Polymer Electrolyte Membrane Fuel Cell Using Un-Assisted Cold Start Strategy.” *International Journal of Hydrogen Energy* 45, no. 58 (2020): 34048–57. https://doi.org/10.1016/j.ijhydene.2020.09.075.

[27] Lamibrac, A., J. Roth, M. Toulec, F. Marone, M. Stampanoni, and F. N. Büchi. “Characterization of Liquid Water Saturation in Gas Diffusion Layers by X-Ray Tomographic Microscopy.” *Journal of The Electrochemical Society* 163, no. 3 (2015). https://doi.org/10.1149/2.0401603jes.

[28] Zenyuk, Iryna V., Dilworth Y. Parkinson, Gisuk Hwang, and Adam Z. Weber. “Probing Water Distribution in Compressed Fuel-Cell Gas-Diffusion Layers Using X-Ray Computed Tomography.” *Electrochemistry Communications* 53 (2015): 24–28. https://doi.org/10.1016/j.elecom.2015.02.005.

[29] Zenyuk, Iryna V., Adrien Lamibrac, Jens Eller, Dilworth Y. Parkinson, Federica Marone, Felix N. Büchi, and Adam Z. Weber. “Investigating Evaporation in Gas Diffusion Layers for Fuel Cells with X-Ray Computed Tomography.” *The Journal of Physical Chemistry C* 120, no. 50 (2016): 28701–11. https://doi.org/10.1021/acs.jpcc.6b10658.

[30] Battrell, Logan, Ning Zhu, Lifeng Zhang, and Ryan Anderson. “Transient, Spatially Resolved Desaturation of Gas Diffusion Layers Measured via Synchrotron Visualization.” *International Journal of Hydrogen Energy* 43, no. 24 (2018): 11234–43. https://doi.org/10.1016/j.ijhydene.2018.05.017.

[31] Kim, Seung-Gon, and Sang-Joon Lee. “Investigation of Water Distribution in a Polymer Electrolyte Fuel Cell Using X-Ray Imaging Technique.” *ASME 2009 7th International Conference on Nanochannels, Microchannels and Minichannels*, 2009. https://doi.org/10.1115/icnmm2009-82290.

[32] Manke, I., Ch. Hartnig, M. Grünerbel, W. Lehnert, N. Kardjilov, A. Haibel, A. Hilger, J. Banhart, and H. Riesemeier. “Investigation of Water Evolution and Transport in Fuel Cells with High Resolution Synchrotron x-Ray Radiography.” *Applied Physics Letters* 90, no. 17 (2007): 174105. https://doi.org/10.1063/1.2731440.

[33] Kim, Seung-Gon, and Sang-Joon Lee. “Tomographic Analysis of Porosity Variation in Gas Diffusion Layer under Freeze-Thaw Cycles.” *International Journal of Hydrogen Energy* 37, no. 1 (2012): 566–74. https://doi.org/10.1016/j.ijhydene.2011.09.052.

[34] Kim, Seung Gon, and Sang Joon Lee. “Quantitative Visualization of a Gas Diffusion Layer in a Polymer Electrolyte Fuel Cell Using Synchrotron X-Ray Imaging Techniques.” *Journal of Synchrotron Radiation* 20, no. 2 (2013): 286–92. https://doi.org/10.1107/s0909049513001659.

[35] Ince, Utku U., Henning Markötter, Michael G. George, Hang Liu, Nan Ge, Jongmin Lee, Saad S. Alrwashdeh, et al. “Effects of Compression on Water Distribution in Gas Diffusion Layer Materials of PEMFC in a Point Injection Device by Means of Synchrotron X-Ray Imaging.” *International Journal of Hydrogen Energy* 43, no. 1 (2018): 391–406. https://doi.org/10.1016/j.ijhydene.2017.11.047.

[36] Markötter, H., R. Alink, J. Haußmann, K. Dittmann, T. Arlt, F. Wieder, C. Tötzke, et al. “Visualization of the Water Distribution in Perforated Gas Diffusion Layers by Means of

Synchrotron X-Ray Radiography." *International Journal of Hydrogen Energy* 37, no. 9 (2012): 7757–61. https://doi.org/10.1016/j.ijhydene.2012.01.141.

[37] Battrell, Logan, Virat Patel, Ning Zhu, Lifeng Zhang, and Ryan Anderson. "Imaging of the Desaturation of Gas Diffusion Layers by Synchrotron Computed Tomography." *Journal of Power Sources* 416 (2019): 155–62. https://doi.org/10.1016/j.jpowsour.2019.01.089.

[38] Oberholzer, P., P. Boillat, R. Siegrist, R. Perego, A. Kästner, E. Lehmann, G. G. Scherer, and A. Wokaun. "Cold-Start of a PEFC Visualized with High Resolution Dynamic In-Plane Neutron Imaging." *Journal of The Electrochemical Society* 159, no. 2 (2011). https://doi.org/10.1149/2.085202jes.

[39] Otsuki, Yota, Yusuke Tamada, Shoki Inoue, Kaito Shigemasa, and Takuto Araki. "Measurement of Solidification Heat from Supercooled Water Freezing during PEFC Cold Start and Visualization of Ice Distribution." *International Journal of Hydrogen Energy* 45, no. 31 (2020): 15600–15610. https://doi.org/10.1016/j.ijhydene.2020.04.004.

[40] Kim, Jongrok, Junho Je, Massoud Kaviany, Sang Young Son, and Moo Hwan Kim. "Visualization of GDL Deformation by Freezing of Water Using X-Ray Radiography." *ASME 2010 8th International Fuel Cell Science, Engineering and Technology Conference: Volume 1*, 2010. https://doi.org/10.1115/fuelcell2010-33281.

[41] Mayrhuber, Immanuel, Federica Marone, Marco Stampanoni, Thomas J. Schmidt, and Felix N. Büchi. "Fast X-Ray Tomographic Microscopy: Investigating Mechanisms of Performance Drop during Freeze Starts of Polymer Electrolyte Fuel Cells." *ChemElectroChem* 2, no. 10 (2015): 1551–59. https://doi.org/10.1002/celc.201500132.

[42] Herrera, O.E., D.P. Wilkinson, and W. Mérida. "Anode and Cathode Overpotentials and Temperature Profiles in a PEMFC." *Journal of Power Sources* 198 (2012): 132–42. https://doi.org/10.1016/j.jpowsour.2011.09.042.

[43] “NE-1000 Series of Programmable Syringe Pumps.” SyringePump.com. New Era Pump Systems Inc. April 2016. www.syringepump.com/download/NE-1000 Syringe Pump User Manual.pdf.

[44] Rashapov, Rinat R., Jonathan Unno, and Jeff T. Gostick. “Characterization of PEMFC Gas Diffusion Layer Porosity.” *Journal of The Electrochemical Society* 162, no. 6 (2015). https://doi.org/10.1149/2.0921506jes.

[45] “SIGRACET ® GDL 34 & 35 Series Gas Diffusion Layer.” Nafion Store. nafionstore-us.americommerce.com/Shared/SGL-GDL_34-35.pdf.

[46] Wysokinski, Tomasz W., Dean Chapman, Gregg Adams, Michel Renier, Pekka Suortti, and William Thomlinson. “Beamlines of the Biomedical Imaging and Therapy Facility at the Canadian Light Source—Part 1.” *Nuclear Instruments and Methods in Physics Research Section A: Accelerators, Spectrometers, Detectors and Associated Equipment* 582, no. 1 (2007): 73–76. https://doi.org/10.1016/j.nima.2007.08.087.

[47] Vogelgesang, Matthias, Suren Chilingaryan, Tomy dos_Santos Rolo, and Andreas Kopmann. “UFO: A Scalable GPU-Based Image Processing Framework for On-Line Monitoring.” *2012 IEEE 14th International Conference on High Performance Computing and Communication & 2012 IEEE 9th International Conference on Embedded Software and Systems*, 2012. https://doi.org/10.1109/hpcc.2012.116.

[48] Vogelgesang, Matthias, Tomas Farago, Thilo F. Morgeneyer, Lukas Helfen, Tomy dos Santos Rolo, Anton Myagotin, and Tilo Baumbach. “Real-Time Image-Content-Based Beamline Control for Smart 4D X-Ray Imaging.” *Journal of Synchrotron Radiation* 23, no. 5 (2016): 1254–63. https://doi.org/10.1107/s1600577516010195.

Chapter 4. Visualizing Water Desaturation in Frozen Gas Diffusion Layers with Flow Field Segmentation via Synchrotron X-ray Radiography

The contents of this chapter have been published at *Frontiers in Energy Research*.

Citation information:

Zhang, Yuzhou, Ryan Anderson, Ning Zhu, and Lifeng Zhang. "Visualizing Water Desaturation in Frozen Gas Diffusion Layers with Flow Field Segmentation via Synchrotron X-ray Radiography." *Frontiers in Energy Research*, 2021. https://doi.org/ 10.3389/fenrg.2021.677685.

Contribution of the MSc student

The experiments, data analysis, and manuscript preparation were performed by Yuzhou Zhang. Ning Zhu provided technical support in synchrotron related problems. Lifeng Zhang and Ryan Anderson provided technical and editorial guidance through the research and manuscript preparation. Lifeng Zhang also provided supervision through the research.

Contribution of this chapter to the overall study

In this chapter, the thawing and desaturation process in a cold-start GDL was visualized via synchrotron X-ray imaging and quantitatively analyzed within a serpentine shape channel flow field. Multiple segmentation levels were applied on the GDL area based on the flow field geometry underneath. Studies on the localized areas showed how the air purging rate, purging distance, flow field geometry affected the water transport behavior during the GDL thawing and desaturation processes.

4.1 Abstract

Synchrotron X-ray tomography images were used to study dynamic, regional water transfer behavior in the gas diffusion layer (GDL) during thawing and desaturation processes. Initially saturated, frozen GDLs were thawed and desaturated with air in a serpentine gas flow channel. On-the-fly (OTF) high speed CT scans via synchrotron X-ray allowed the capture of consecutive water transfer inside the GDL under the cold start-up gas purging condition. Desaturation data of Sigracet® 35AA GDLs with 3 superficial gas velocities (2.88-5.98 m/s) were selected for analysis. Multiple spatial segmentation levels based on the flow field geometry,

including channel vs. rib, individual channels and ribs, and smaller sections in each channel and rib, were applied to the in-plane direction to study the GDL regional thawing and desaturation behaviors. Each segmentation volume had a similar desaturation pattern in general; however, water distribution and desaturation show heterogeneity over the GDL domain, as well as relation with factors including the flow field geometry, air traveling distance, and initial saturation level. These data from the segmentation analysis expand the knowledge of localized water transfer behavior during the cold start thawing process. These data can also provide valuable information for future cold start modeling and help in optimizing the PEM fuel cell flow field design.

Keywords: PEM fuel cell, gas diffusion layer, cold start-up, saturation, X-ray radiography, flow field, segmentation

4.2 Introduction

Proton-exchange membrane fuel cells (PEM fuel cells) have gained increased interest as one of the clean energy solutions for small scale applications. Owing to their high energy efficiency, zero emissions, and simplicity in operation, PEM fuel cells are considered as a promising clean energy alternative in future automobiles to replace the fossil fuel engines [1-7]. One of the main challenges to a successful commercialized PEM fuel cell product is water management, where the water generated from the electrochemical reaction and removed by the cell needs to be balanced in order to maintain the optimized hydration level through the entire cell. Excess water may cause blockages, which limit the gas transfer to the catalyst layer; insufficient water may cause membrane dehydration. Both issues can lead to performance loss and even irreversible cell degradation in the long term [8,9].

The gas diffusion layers (GDLs) play a crucial role in PEM fuel cell water management. As a part of the membrane electrode assembly (MEA), the GDL is a thin layer of porous media with porosity of 75 – 90 % placed between the channel and the catalyst layer, which functions as the bridge of mass transfer between these layers [10]. Poor water management, especially water flooding in the GDL can limit or even prevent the reactants from reaching the catalyst and membrane. It could become a more serious problem in the operation under the subzero temperature [5,6,8]. The frozen water in the MEA could completely block the transport of the reactant streams and cause gas starvation, which may lead to carbon corrosion, catalyst degradation, voltage reversal, and in the long term, lifetime reduction and cell failure [11-15].

Therefore, removing excess water in the GDL is essential for low operating temperature. Due to the difficulty in studying the water transfer phenomenon in this small scale of porous media, which also involves heat transfer and phase change, cold-start operation has become one of the main challenges in PEM fuel cell commercialization in the automobile industry. Pressurized dry gas purging on the anode/cathode side is considered as a common solution for the cold-start problem [16,17].

For experimental approaches, visualization via X-ray or neutron imaging is one of the methods used in GDL water management studies. As the high energy beam penetrates the materials, the inner structure of the sample can be revealed with contrast difference based on the material properties without cutting through the sample. X-ray imaging differentiates the material via density difference, which can support both qualitative and quantitative studies on GDL structure and liquid water distribution when combined with the computed tomography technique (CT). Compared with the lab-based X-ray imaging system, the high photon flux from synchrotron X-ray provides high spatial and temporal resolution, making it possible to capture the dynamic water transfer process in the GDL [18]. Using X-ray CT data, Lamibrac et al. [19] characterized the liquid water saturation in the microporous layer (MPL) coated GDLs as a function of the capillary pressure. Ince et al. [20] showed that the in-plane water distribution in the porous structures of both MPL and GDL increased as the GDL compression level increased. Markötter et al. [21] visualized the increased hydrophilicity in water distribution around the holes of perforated GDLs. For dynamic water transfer processes, Zenyuk et al. [22] visualized the water evaporation in several GDLs with gas flow rates of 200 and 600 ml/min at 30 °C. The desaturation process in the GDL was also visualized by Battrell et al. [23,24] for both global and localized GDL areas, with the gas flow rate at 50 ml/min.

In the literature, several studies were conducted on GDL visualization with subzero operating temperatures or GDL freezing/thawing processes. Otsuki et al. [25] measured the solidification heat from supercooled water using thin-film thermocouples and visualized the ice distribution via X-ray CT after several cold-start operations. Kim et al. [26] visualized the GDL structure deformation after freezing the pre-saturated GDL using X-ray tomography. By in-situ visualization of water production and water transfer via synchrotron X-ray CT, Mayrhuber et al. [27] investigated the mechanism of the performance drop during the cold-start operation of PEM

fuel cells. Kim et al. [28,29] quantitively measured the heterogeneous distribution of the GDL's porosity using synchrotron X-ray CT, and studied the GDL structures with 3D reconstruction after the GDLs experienced freezing/thawing cycles. As most of the X-ray visualization studies involving subzero temperatures focused on the GDL structure after the freezing/thawing cycles, neutron imaging has been used in several studies to visualize the dynamic process in the cold-start condition. Siegwart et al. [8] visualized the dynamic phase change of water during the isothermal PEM fuel cell cold-start and successfully distinguished ice from liquid water via contrast difference using 2D neutron imaging. Water accumulation has been visualized by Oberholzer et al. [30] during the isothermal cold-start using in-plane neutron imaging.

Flow field geometry is one of the important elements of PEM fuel cell design, which has significant impact on aspects such as cell performance and water management. Hence, understanding the effects of flow field geometry is critical in optimizing the design and improving the performance and water management ability. Spernjak et al. [31, 32] experimentally investigated the liquid water formation and transport in a single-serpentine PEM fuel cell, and also compared the liquid water dynamics in parallel, serpentine, and interdigitated flow fields using neutron imaging and digital camera. Battrell et al. [24] quantitatively visualized the water removal in the GDL with serpentine gas channels, considering the effects of flow field geometry. Ding et al. [33] compared the cell performances of a parallel, interdigitated, and serpentine flow field with normal and wavelike channels using a three-dimensional, two-phase, non-isothermal model. Yin et al. [34] numerically investigated the liquid water droplet movement at the U-turn of the serpentine channel. Kerkoub et al. [35] used a three-dimensional CFD model to study the effects of the channel to rib width ratio for the PEM fuel cell with parallel, serpentine, and interdigitated flow fields.

In summary, although numerous studies have experimentally or numerically investigated the PEM fuel cell and GDL water management, there is still a lack of a clear understanding of the water transfer phenomenon in this porous media. High quality visualization could provide valuable information for modeling and numerical studies. However, most of the existing visualization research studied the water behavior with the cell in an idle state to increase the exposure time. Using the low energy monochromatic beam with long exposure time in X-ray imaging can increase the quality of spatial resolution and material contrast, but the duration of

each scan is too long to capture the water dynamics. Furthermore, in studying the dynamic water behavior with cold-start conditions, although neutron imaging is commonly used for its high sensitivity to ice and liquid water, it can only provide low resolution images due to apparatus limitation. It can be seen that the dynamic processes of freezing, thawing and water movement in the cold-start GDL are not well understood. Motivated by these challenges, the thawing and desaturation process of a pre-saturated frozen GDL was 3-D visualized using high-speed synchrotron X-ray CT and analyzed both qualitatively and quantitively in this work. Multiple GDL samples (Sigracet® 35AA and 35BA graphite GDLs) were studied with a serpentine flow field and the air purging rate at 10, 20, 30 ml/min during the desaturation. Continuing previous work [36], which studied the global desaturation profile and heterogeneity across the entire GDL domain, this research focuses on the localized desaturation and water behaviors in smaller scale to study the effects of flow field on the GDL water management. This work provides valuable data for the modeling community for simulation of the water transfer and the freezing/thawing process in the GDL. These data can also be useful for future design of GDLs, flow fields, and cold-start strategies to improve the overall water management of PEM fuel cells.

4.3 Methodology

This research used the same protocols and setups as a previous experiment [36] and were discussed there in detail. A summary is included in the following section along with the changes and improvements.

4.3.1 Experiment protocols

The GDL sample was initially saturated by injecting liquid water at 0.05 ml/min using a syringe pump. The saturated GDL was then transferred into the test cell and an X-ray CT scan was performed. After this point, the GDL sample remained in the test cell untouched until the end of this experimental trial to minimize the position change in each scan. The GDL was frozen in a -80 °C freezer for 20 minutes to simulate the rapid ice formation in the GDL during the subzero temperature. Then, the test cell was mounted on the CT rotation stage and the scans were performed in 2-minute intervals for a total of 30 minutes, with ambient temperature dry air constantly purging the cell at the rate of 10 ml/min, 20 ml/min or 30 ml/min depending on the experimental conditions, corresponding to 2.88 m/s, 4.26 m/s and 5.98 m/s superficial gas velocity in the gas channel. A CT scan was captured for baseline GDL porosity on the dry state

sample at the end of each experiment after a 5-minute air purge was applied. Two GDL samples from the same product series, Sigracet® 35AA and 35BA, were used in the experiment, where the 35BA has additional 5 % PTFE loading for higher hydrophobicity [37].

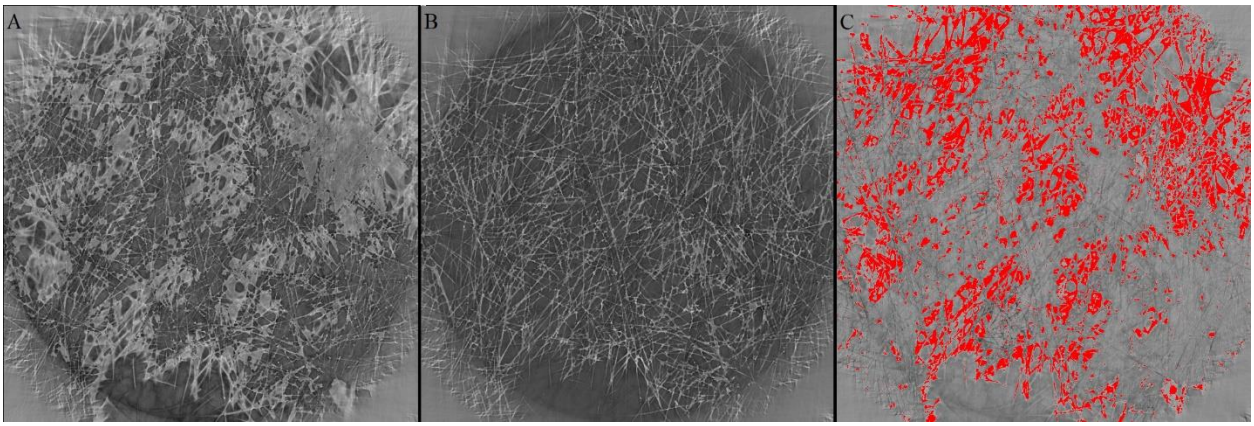

Figure 4.1. Synchrotron X-ray reconstructed slices for 35AAGDL with 20 ml/min air purging rate at A) 0 minute thawing process, B) dry state. C) Total water content (highlight in red) after segmentation via image subtraction.

Raw 2D projections were reconstructed with ultra-fast imaging and online reconstruction - Karlsruhe Institute of Technology (UFO-KIT), where background correction and phase retrieval were applied during the scan as well as during the reconstruction to enhance the image quality and reduce the noise [38,39]. The reconstructed images (32-bit, black-and-white) were imported to ImageJ 1.52a for image processing, segmentation, and calculation. The sample images of the reconstructed slices are shown in Figure 4.1-A and B, where the bright sections represent the water/GDL structure mixture, and the dark sections represent the empty porous space. The segmentation was done by first separating the water/GDL structure mixture from the total volume via the large contrast difference between the unoccupied space (air) and materials due to their significant density difference. Due to the small contrast difference between the GDL fiber, liquid water, and ice, previous segmentation method could not be applied to separate each other. Therefore, the water content was segmented from the GCL carbon fiber by subtracting the volume with the GDL structure captured from the dry state baseline, where the liquid water and ice were both included in the total water content, shown in Figure 4.1-C, for further calculation. Using the quantitative data extracted from the segmented images, the percentage-saturation of the GDL was calculated as the volume of water content divided by the total pore volume in the

dry state GDL. The desaturation rate of the GDL was calculated as the change in the volume of water content over 4 minutes divided by cross sectional area of the GDL. Previous research showed the heterogeneity in water distribution during the initial saturation, and the impacts of the initial saturation on the magnitude of desaturation rate, which could be more noticeable when zooming into the localized level. Therefore, the desaturation data was additionally normalized with the local initial saturation level, which transformed into the percentage removal rate of the initial residual water in that GDL area. The normalized percentage water removal rate was calculated as averaged desaturation rate over 4 minutes divided by the volume of initial water content.

4.3.2 Synchrotron setups and cell design

All the experiments for this research were performed at the Bio-Medical Imaging and Therapy (BMIT) 05B1-1 beamline in the Canadian Light Source Inc., the 3rd generation synchrotron facility located in Saskatoon, Canada [40]. 2000 projections were captured in 10 seconds during each CT scan, with the Field of View (FOV) set as 10 mm x 1.5 mm and the pixel size set as 5.3 μm. 20 keV high photon flux filtered white beam and the detector with the combination of a high-speed camera DIMAX HS4 (PCO) and a beamline monitor AA40 (HAMAMATSU) ensured the high CT capture speed and the high image quality. Phase contract method was applied to enhance the image quality by placing the detector 0.4 m away from the test cell.

The test cell used in this experiment simulated the water transfer in the GDL and channel on the cathode side of a single PEM fuel cell unit. To minimize the effects of the test cell during the experiment, polyether ether ketone (PEEK) was selected as the cell material for its low X-ray absorption rate and high durability. When the top and bottom parts of the test cell shown in Figure 4.2-A and B assembled, the GDL sample was placed between the 40 mm serpentine shape gas/water channels, shown in Figure 4.2-C, and sealed with the rubble gaskets at the edge.

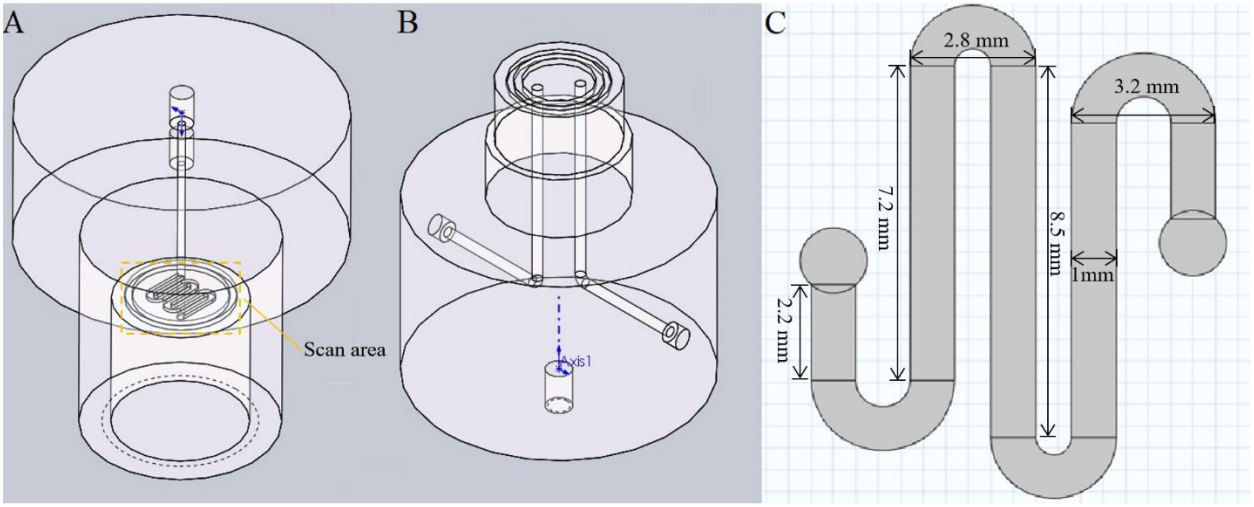

Figure 4.2. 3D schematics of the test cell A) top and B) bottom parts; C) flow channel design with dimension.

4.3.3 Flow field segmentation

This research focuses on localized water behavior during the thawing and desaturation process, and the effects related to the flow field geometry. For doing so, the GDL area underneath the channel and the rib was segmented in 3 different levels, and the GDL thawing and desaturation process was studied within each individual area. In the first level, channel/rib was studied as a whole, where the channel area was a continuous section with 5 individual channels and 4 bends, and the rib area contains all 4 ribs between the channels. For the next segmentation level, each individual channel (C), bend (B), and rib (R) is isolated from the whole channel/rib area as shown in Figure 4.3-A. In the third level, each long channel and rib is evenly separated into 3 smaller sections, as shown in Figure 4.3-B, where the short channels, short ribs, and bends remain in the same segmentation as in the second level. The number in the naming convention of the segmented sections is set as an increment order along the direction of the air purging flow.

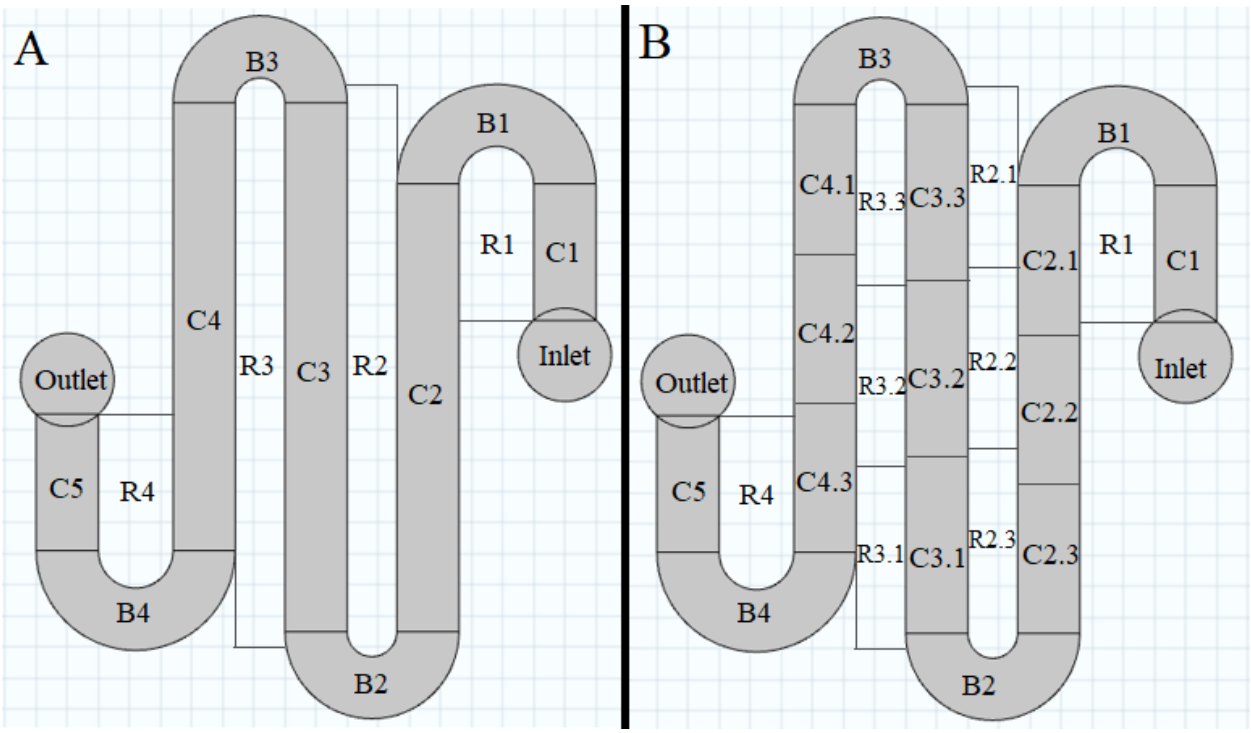

Figure 4.3. Schematic showing the geometry and the naming convention for A) second segmentation level and B) third segmentation level.

4.4 Results and discussion

The in-plane saturation profiles and desaturation rates are examined in different segmentation levels within the GDL area, which include the whole channel/rib areas, individual channels/ribs, and smaller sections within a single channel/rib. This work investigated how the flow filed geometry affected the thawing and desaturation process in the frozen GDLs. Also, according to previous research, this difference in GDL hydrophobicity (difference in 35AA and 35BA) has insignificant impact on the thawing and desaturation process, and would almost only affect the overall GDL initial saturation level. Therefore, the data analysis focused on comparing the saturation profiles and desaturation rates in different segmentations within the same experimental trial.

4.4.1 Saturation profile and desaturation rate – whole channel/rib areas

The first analysis was performed under the coarser segmentation of the 3 levels. The whole channel domain is the continuous area and includes all the 5 channel segments and 4 bends, and the whole rib domain is the sum of all the 4 rib areas. The channel vs. rib saturation profiles and desaturation rates for 35AA and 35BA GDLs with 10, 20, and 30 ml/min air purging

rates are shown in Figure 4.4. Like the thawing and desaturation process for the overall GDL domain, the saturation profiles and desaturation rates at the large scale in both channel and ribs show a similar trend in all the cases. From 0 to 10 minutes, the temperature of the GDL increased but remained in frozen condition, indicated by the flat curves in the saturation plots and close to zero desaturation rates. From 5 to 15 minutes, ice thawing occurred with an increased amount of water removed the from GDL. Therefore, the desaturation rates started to increase. The peak in the desaturation profile indicates the completion of the thawing process at around 15 minutes. For the rest of the purging process, the desaturation rates continue to decrease until most of the water content is removed from the GDL, as the desaturation rates drop to almost 0 µL cm^{-2} s^{-1}.

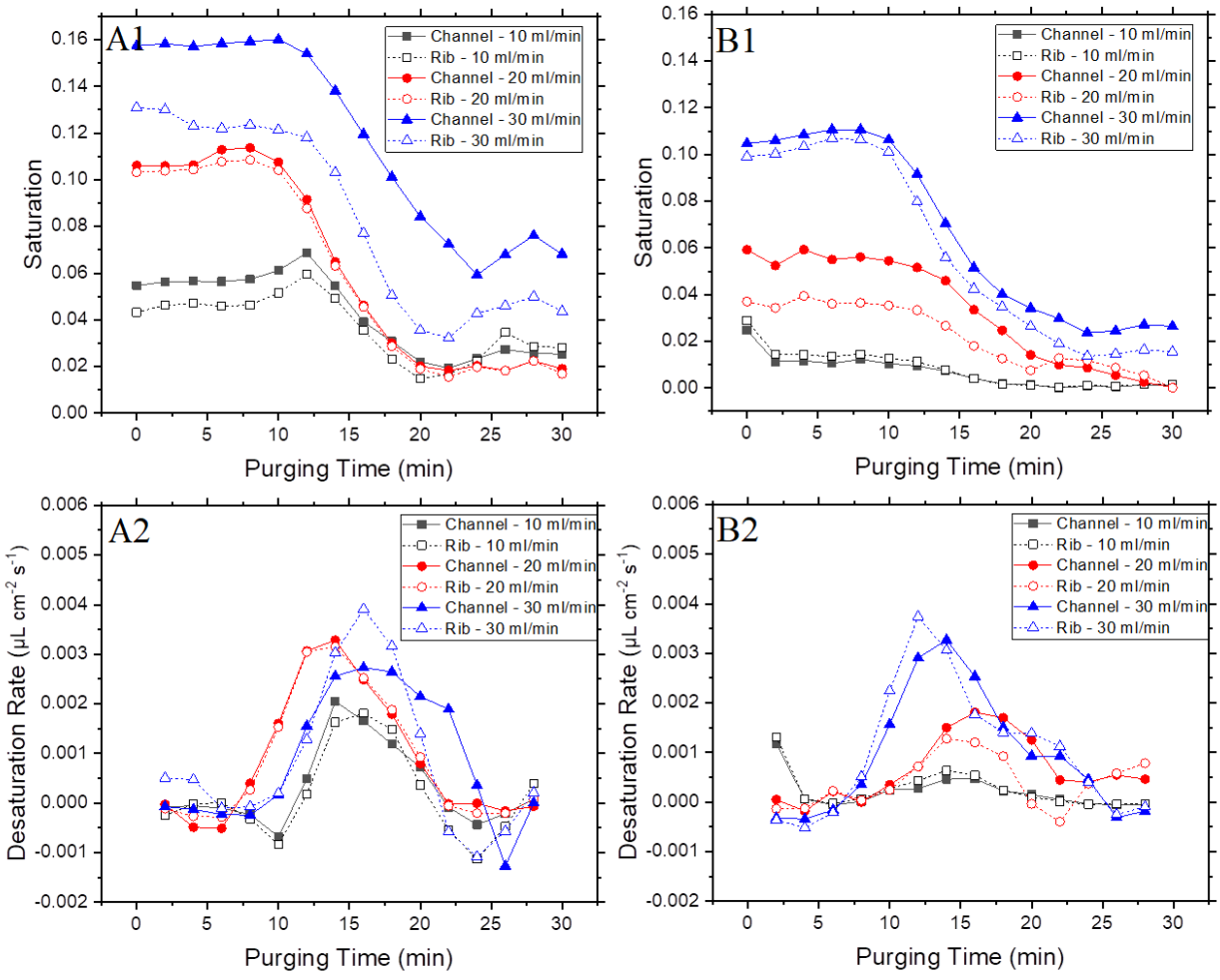

Figure 4.4. Dynamic 1) saturation profiles and 2) desaturation rates for A) 35AA GDL B) 35BA GDL over both whole channel and ribs domains, with 10, 20, and 30 ml/min air purging rates.

By comparing the desaturation rates for the channel and the ribs within the individual experimental cases, it is observed that at the large scale, the difference in the thawing and desaturation process is not significant between the two segmented domains. The durations of the same phase in the air purging process are similar or even identical for the channel and ribs areas in the same experimental case. For 35AA GDL with a 20 ml/min air purging rate, the desaturation curves for the channel and ribs completely overlap, where the difference in averaged desaturation rates is only 1.08 %. The differences in the channel and ribs desaturation profiles for 35AA GDL with 30 ml/min and 35BA GDL with 20 ml/min could be caused by other factors rather than the flow field geometry such as GDL initial saturation level. For instance, the initial saturation differences in the channel and the ribs for 35AA with 30 ml/min and 35BA with 20 ml/min are 16.8 % and 37.5 %, respectively, and the initial saturation difference is only 2.78 % for 35AA with 20 ml/min air purging rate.

4.4.2 Saturation profile and desaturation rate – individual channels/ribs

To investigate localized saturation and desaturation rates in the flow field, the individual channels, bends, and ribs were further divided in the next segmentation level as shown in Figure 4.3-A. Previous research showed that a high level of heterogeneity could occur in the saturation across the GDL domain, and this uneven water distribution can affect the desaturation rates in those areas, where the magnitude of the desaturation rates appears to be proportional to the initial saturation level. This effect becomes more significant when zooming into smaller GDL area. To minimize this effect, the desaturation rate values in each segmented area were normalized using the initial saturation values in those sections, and the desaturation rates were transformed into the percentage initial water removal rates. After normalization, the channels, bends, and ribs water removal rates for 35AA GDL at a 20 ml/min air purging rate are shown in Figure 4.5-A, B, and C, respectively. No significant difference could be found between the magnitudes of the water removal rates in each section. However, it can be clearly seen that the peaks of the desaturation curves shift to earlier times in segments closer to the air inlet (a shorter purging distance). The humidity of the purging air increases as it travels along the channel from the inlet to the outlet, and the thawing and desaturation of the GDL slows down during this process. For instance, the full thawing point of B4 came 5 minutes later than B1, which has approximately 28 mm purging distance longer than B1.

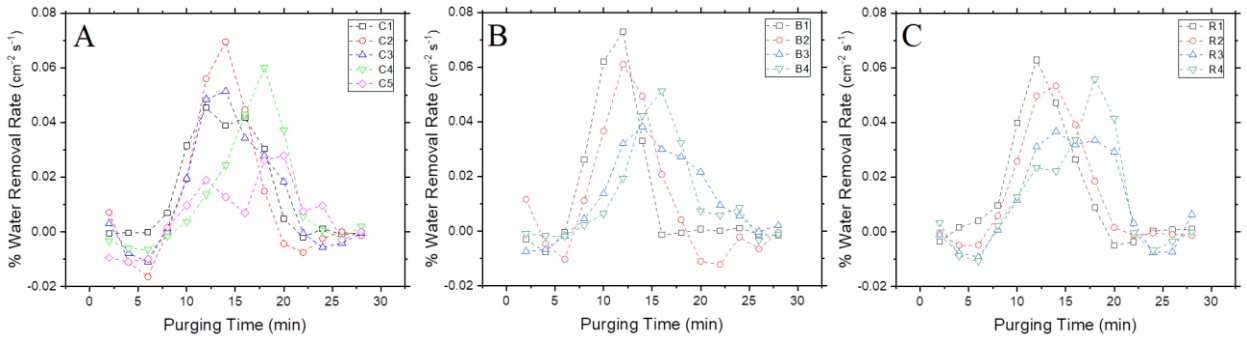

Figure 4.5. Normalized percentage water removal rates profiles for 35AA GDL with 20 ml/min air purging rate underneath the A) channels, B) bends, C) ribs.

4.4.3 Saturation profile and desaturation rate – channel and rib segmentation

Each long channel and rib were evenly divided into 3 rectangular sections at finer segmentation level shown as Figure 4.3-B. Taking 35AA GDL with 20 ml/min air purging rate as an example, the saturation profiles of all the segments are presented on surface plots shown in Figure 4.6, where the geometries on the plots represent the actual flow field geometries in Figure 4.3-B. For better demonstration, the saturation profiles are converted into the value of percentage water relative to the initial residual water in each section. Heterogeneity in the thawing and desaturation process were observed through the entire GDL area. From 0 to 8 minutes, the saturation level in most of the GDL areas increased and exceeded their initial saturation values. This increase in the water volume may be caused by the combination of the volume expansion from the ice thawing, and the liquid water intrusion from the water droplets and thin films attached to the bottom surface of the GDL due to the through-plane pressure difference caused by the purging flow.

From 8 to 16 minutes, rapid water removal occurs in all the segmented areas. The channel and rib segments closer to the outlet of the purging air desaturate slower than the segments near the inlet. At 24 minutes, as 78.3 % of the segmented areas have the saturation drop below 30 % of the initial water content, C2.3, C4.2, C5, R3.1, and R3.2 desaturate slower than other sections. C4.2 was not considered as the slow desaturation region due to its low initial saturation level at 2.56 %. Other than that area, the slow desaturation regions could appear randomly in both channel and rib areas, but had a higher chance to appear near the outlet than the inlet. From 20 to 28 minutes, desaturation across all the areas slowed down with almost no

significant change in the saturation level, and the water removal rates in the slow desaturation regions did not increase as the water removal process finished for the rest of the areas.

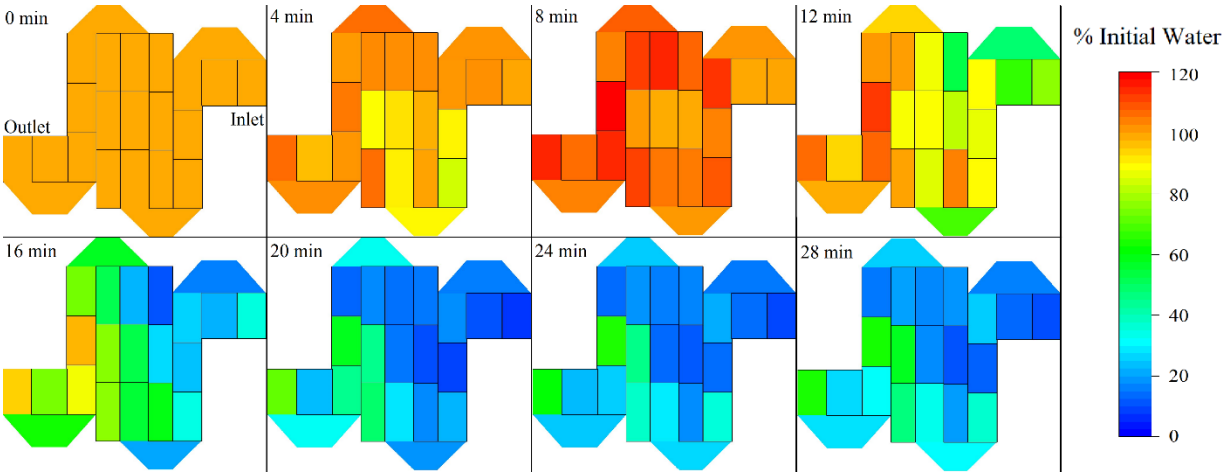

Figure 4.6. Spatial saturation colormaps include all the segmentations in the 35AA GDL with 20 ml/min air purging rate experiment.

In studying the effect of purging distance, the percentage water removal rates of the finer segmentations for each long channel and rib are shown in Figure 4.7. Heterogeneity becomes more obvious in the smaller scale. Different from the results in the second segmentation level, the effect of purging distance was not clearly observed within C2, C3, and R3. Also, C3.3 and R3.3 appeared to be outliers that had higher water removal rates and a faster thawing process than the other sections within the same channel/rib. It indicates that other localized factors such as GDL structure, permeability and pore size could potentially influence the thawing and desaturation process in the GDL.

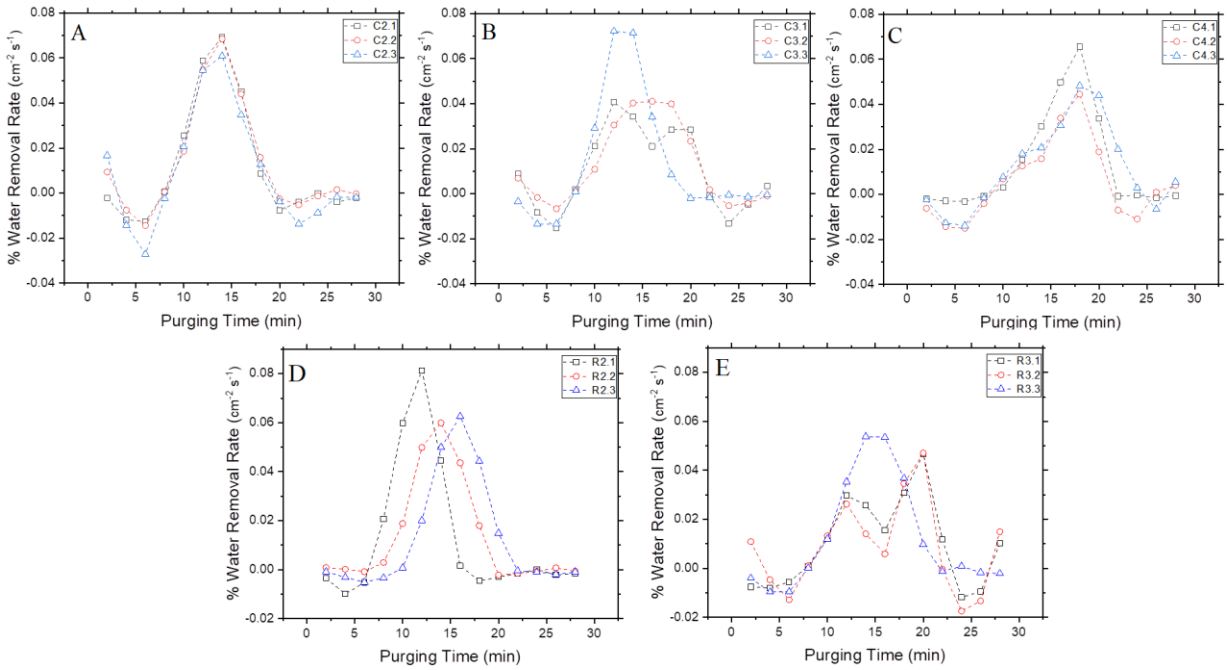

Figure 4.7. Normalized percent water removal rates profiles for 35AA GDL with 20 ml/min air purging rate for segmentations underneath A) channel 2, B) channel 3, C) channel 4, D) rib 2, E) rib 3.

In studying the effect of flow field geometry on the thawing and desaturation process, a comparison of the water removal rates in a mixed area of channels, bend, and rib was conducted and results are shown in Figure 4.8. To isolate the effect of purging distance, 4 neighboring sections, C3.3, B3, R3.3, and C4.1 were selected, which form a continuous U-shape channel area plus the rib area between the two straight channels. Two straight channels, C3.3 and C4.1, have the fastest and slowest thawing process among the four areas respectively, where the bend and rib areas B3 and R3.3 laid in between. Comparing with the straight channel in Figure 4.7, the U-shape channel area including C3.3, B3, and C4.1 has a similar purging distance. However, the difference of the thawing process duration in the U-shape channel is significantly larger than the straight channel, which shows approximately 5 minutes difference on the GDL full thawing points, indicates that the bend structure of the U-shape/serpentine shape channel could slow down the thawing and desaturation process for the areas after the structure. Combined with the purging distance factor, the longer the purging air travels along the serpentine shape channel, the longer it would take for the ice under this channel area to thaw and be removed.

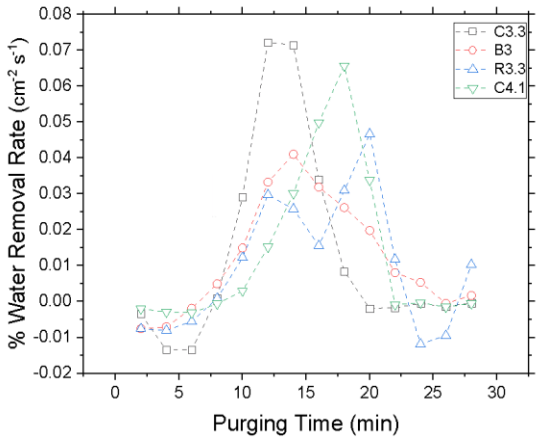

Figure 4.8. Normalized percent water removal rates profiles for 35AA GDL with 20 ml/min air purging rate underneath a U-shape channel area.

4.5 Conclusions

GDL thawing and desaturation processes were visualized and analyzed both qualitatively and quantitatively on multiple segmentation levels under air purging conditions via synchrotron X-ray CT. Three desaturation phases were noted in the desaturation profiles in the large scale of GDL domain and locally in the smaller segmented areas: GDL warmup, partial thawing with water removal, and desaturation after complete thawing. At larger scale, the relationship between the desaturation and the channel/rib geometry was not clearly observed. Zooming into smaller segment levels, both the temporal desaturation profiles and the spatial saturation colormaps show that the purging distance, flow field geometry, and the initial saturation level play important roles in the GDL thawing and desaturation process, where longer purging distance and bend channel structures decreased the thawing speed. Besides these factors, heterogeneity in desaturation was found across the GDL, even for the neighboring areas. These results also show the difference in the thawing and desaturation process between the global and the local GDL domain, which indicates that the water behaviors in localized areas could be the key in solving the water management problems for the PEM fuel cell. These results provide valuable information for understanding the GDL water management during cold-start and could be used in optimizing the PEM fuel cell flow field design.

4.6 Acknowledgements

LFZ and RA acknowledge the support from their respective universities, the University of Saskatchewan and Montana State University. LFZ also acknowledges financial support from Natural Sciences and Engineering Research Council of Canada. Experiments and image processing described in this paper were performed at the BMIT facility at the Canadian Light Source, which is supported by the Canada Foundation for Innovation, Natural Sciences and Engineering Research Council of Canada, the University of Saskatchewan, the Government of Saskatchewan, Western Economic Diversification Canada, the National Research Council Canada, and the Canadian Institutes of Health Research.

4.7 References

[1] Spiegel, Colleen. *PEM Fuel Cell Modeling and Simulation Using Matlab*. Burlington: Elsevier Science, 2011.

[2] Hardman, Scott, Robert Steinberger-Wilckens, and Dan van der Horst. "Disruptive Innovations: The Case for Hydrogen Fuel Cells and Battery Electric Vehicles." *International Journal of Hydrogen Energy* 38, no. 35 (2013): 15438–51. https://doi.org/10.1016/j.ijhydene.2013.09.088.

[3] Anderson, Ryan, Lifeng Zhang, Yulong Ding, Mauricio Blanco, Xiaotao Bi, and David P. Wilkinson. "A Critical Review of Two-Phase Flow in Gas Flow Channels of Proton Exchange Membrane Fuel Cells." *Journal of Power Sources* 195, no. 15 (2010): 4531–53. https://doi.org/10.1016/j.jpowsour.2009.12.123.

[4] Andersson, M., S.B. Beale, M. Espinoza, Z. Wu, and W. Lehnert. "A Review of Cell-Scale Multiphase Flow Modeling, Including Water Management, in Polymer Electrolyte Fuel Cells." *Applied Energy* 180 (2016): 757–78. https://doi.org/10.1016/j.apenergy.2016.08.010.

[5] Amamou, Ali Akrem, Sousso Kelouwani, Loic Boulon, and Kodjo Agbossou. "A Comprehensive Review of Solutions and Strategies for Cold Start of Automotive Proton

Exchange Membrane Fuel Cells." *IEEE Access* 4 (2016): 4989–5002. https://doi.org/10.1109/access.2016.2597058.

[6] Lin, Rui, Yuanming Weng, Xuwei Lin, and Feng Xiong. "Rapid Cold Start of Proton Exchange Membrane Fuel Cells by the Printed Circuit Board Technology." *International Journal of Hydrogen Energy* 39, no. 32 (2014): 18369–78. https://doi.org/10.1016/j.ijhydene.2014.09.065.

[7] Pandian, Meiyappan Siva, Makbul Anwari, Budi Yanto Husodo, and Ayong Hiendro. "Efficiency and Economics Analysis of Proton Exchange Membrane Fuel Cell." *2010 Conference Proceedings IPEC*, 2010. https://doi.org/10.1109/ipecon.2010.5697089.

[8] Siegwart, M., F. Huang, M. Cochet, T. J. Schmidt, J. Zhang, and P. Boillat. "Spatially Resolved Analysis of Freezing during Isothermal PEFC Cold Starts with Time-of-Flight Neutron Imaging." *Journal of The Electrochemical Society* 167, no. 6 (2020): 064510. https://doi.org/10.1149/1945-7111/ab7d91.

[9] Kim, Seung-Gon, and Sang-Joon Lee. "A Review on Experimental Evaluation of Water Management in a Polymer Electrolyte Fuel Cell Using X-Ray Imaging Technique." *Journal of Power Sources* 230 (2013): 101–8. https://doi.org/10.1016/j.jpowsour.2012.12.030.

[10] Safi, Mohammad Amin, Nikolaos I. Prasianakis, John Mantzaras, Adrien Lamibrac, and Felix N. Büchi. "Experimental and Pore-Level Numerical Investigation of Water Evaporation in Gas Diffusion Layers of Polymer Electrolyte Fuel Cells." *International Journal of Heat and Mass Transfer* 115 (2017): 238–49. https://doi.org/10.1016/j.ijheatmasstransfer.2017.07.050.

[11] Chen, Huicui, Xin Zhao, Tong Zhang, and Pucheng Pei. "The Reactant Starvation of the Proton Exchange Membrane Fuel Cells for Vehicular Applications: A Review." *Energy Conversion and Management* 182 (2019): 282–98. https://doi.org/10.1016/j.enconman.2018.12.049.

[12] Li, Pengcheng, Pucheng Fei, Yongling He, and Xing Yuan. “A Starvation Diagnosis Method for a PEM Fuel Cell during Dynamic Loading.” *Gaojishu Tongxin/Chinese High Technology Letters* 23, no. 2 (2013): 189–95. https://doi.org/10.3772/j.issn.1002-0470.2013.02.012.

[13] Liang, Dong, Qiang Shen, Ming Hou, Zhigang Shao, and Baolian Yi. “Study of the Cell Reversal Process of Large Area Proton Exchange Membrane Fuel Cells under Fuel Starvation.” *Journal of Power Sources* 194, no. 2 (2009): 847–53. https://doi.org/10.1016/j.jpowsour.2009.06.059.

[14] Taniguchi, Akira, Tomoki Akita, Kazuaki Yasuda, and Yoshinori Miyazaki. “Analysis of Electrocatalyst Degradation in PEMFC Caused by Cell Reversal during Fuel Starvation.” *Journal of Power Sources* 130, no. 1-2 (2004): 42–49. https://doi.org/10.1016/j.jpowsour.2003.12.035.

[15] Knights, Shanna D, Kevin M Colbow, Jean St-Pierre, and David P Wilkinson. “Aging Mechanisms and Lifetime of PEFC and DMFC.” *Journal of Power Sources* 127, no. 1-2 (2004): 127–34. https://doi.org/10.1016/j.jpowsour.2003.09.033.

[16] Tang, Hong-Yue, Anthony D. Santamaria, John Bachman, and Jae Wan Park. “Vacuum-Assisted Drying of Polymer Electrolyte Membrane Fuel Cell.” *Applied Energy* 107 (2013): 264–70. https://doi.org/10.1016/j.apenergy.2013.01.053.

[17] Tajiri, Kazuya, Chao-Yang Wang, and Yuichiro Tabuchi. “Water Removal from a PEFC during Gas Purge.” *Electrochimica Acta* 53, no. 22 (2008): 6337–43. https://doi.org/10.1016/j.electacta.2008.04.035.

[18] Manke, I., Ch. Hartnig, M. Grünerbel, W. Lehnert, N. Kardjilov, A. Haibel, A. Hilger, J. Banhart, and H. Riesemeier. “Investigation of Water Evolution and Transport in Fuel Cells with High Resolution Synchrotron x-Ray Radiography.” *Applied Physics Letters* 90, no. 17 (2007): 174105. https://doi.org/10.1063/1.2731440.

[19] Lamibrac, A., J. Roth, M. Toulec, F. Marone, M. Stampanoni, and F. N. Büchi. "Characterization of Liquid Water Saturation in Gas Diffusion Layers by X-Ray Tomographic Microscopy." *Journal of The Electrochemical Society* 163, no. 3 (2015). https://doi.org/10.1149/2.0401603jes.

[20] Ince, Utku U., Henning Markötter, Michael G. George, Hang Liu, Nan Ge, Jongmin Lee, Saad S. Alrwashdeh, et al. "Effects of Compression on Water Distribution in Gas Diffusion Layer Materials of PEMFC in a Point Injection Device by Means of Synchrotron X-Ray Imaging." *International Journal of Hydrogen Energy* 43, no. 1 (2018): 391–406. https://doi.org/10.1016/j.ijhydene.2017.11.047.

[21] Markötter, H., R. Alink, J. Haußmann, K. Dittmann, T. Arlt, F. Wieder, C. Tötzke, et al. "Visualization of the Water Distribution in Perforated Gas Diffusion Layers by Means of Synchrotron X-Ray Radiography." *International Journal of Hydrogen Energy* 37, no. 9 (2012): 7757–61. https://doi.org/10.1016/j.ijhydene.2012.01.141.

[22] Zenyuk, Iryna V., Adrien Lamibrac, Jens Eller, Dilworth Y. Parkinson, Federica Marone, Felix N. Büchi, and Adam Z. Weber. "Investigating Evaporation in Gas Diffusion Layers for Fuel Cells with X-Ray Computed Tomography." *The Journal of Physical Chemistry C* 120, no. 50 (2016): 28701–11. https://doi.org/10.1021/acs.jpcc.6b10658.

[23] Battrell, Logan, Ning Zhu, Lifeng Zhang, and Ryan Anderson. "Transient, Spatially Resolved Desaturation of Gas Diffusion Layers Measured via Synchrotron Visualization." *International Journal of Hydrogen Energy* 43, no. 24 (2018): 11234–43. https://doi.org/10.1016/j.ijhydene.2018.05.017.

[24] Battrell, Logan, Virat Patel, Ning Zhu, Lifeng Zhang, and Ryan Anderson. "Imaging of the Desaturation of Gas Diffusion Layers by Synchrotron Computed Tomography." *Journal of Power Sources* 416 (2019): 155–62. https://doi.org/10.1016/j.jpowsour.2019.01.089.

[25] Otsuki, Yota, Yusuke Tamada, Shoki Inoue, Kaito Shigemasa, and Takuto Araki. "Measurement of Solidification Heat from Supercooled Water Freezing during PEFC Cold

Start and Visualization of Ice Distribution." *International Journal of Hydrogen Energy* 45, no. 31 (2020): 15600–15610. https://doi.org/10.1016/j.ijhydene.2020.04.004.

[26] Kim, Jongrok, Junho Je, Massoud Kaviany, Sang Young Son, and Moo Hwan Kim. "Visualization of GDL Deformation by Freezing of Water Using X-Ray Radiography." *ASME 2010 8th International Fuel Cell Science, Engineering and Technology Conference: Volume 1*, 2010. https://doi.org/10.1115/fuelcell2010-33281.

[27] Mayrhuber, Immanuel, Federica Marone, Marco Stampanoni, Thomas J. Schmidt, and Felix N. Büchi. "Fast X-Ray Tomographic Microscopy: Investigating Mechanisms of Performance Drop during Freeze Starts of Polymer Electrolyte Fuel Cells." *ChemElectroChem* 2, no. 10 (2015): 1551–59. https://doi.org/10.1002/celc.201500132.

[28] Kim, Seung-Gon, and Sang-Joon Lee. "Tomographic Analysis of Porosity Variation in Gas Diffusion Layer under Freeze-Thaw Cycles." *International Journal of Hydrogen Energy* 37, no. 1 (2012): 566–74. https://doi.org/10.1016/j.ijhydene.2011.09.052.

[29] Kim, Seung Gon, and Sang Joon Lee. "Quantitative Visualization of a Gas Diffusion Layer in a Polymer Electrolyte Fuel Cell Using Synchrotron X-Ray Imaging Techniques." *Journal of Synchrotron Radiation* 20, no. 2 (2013): 286–92. https://doi.org/10.1107/s0909049513001659.

[30] Oberholzer, P., P. Boillat, R. Siegrist, R. Perego, A. Kästner, E. Lehmann, G. G. Scherer, and A. Wokaun. "Cold-Start of a PEFC Visualized with High Resolution Dynamic In-Plane Neutron Imaging." *Journal of The Electrochemical Society* 159, no. 2 (2011). https://doi.org/10.1149/2.085202jes.

[31] Spernjak, Dusan, Ajay K. Prasad, and Suresh G. Advani. "Experimental Investigation of Liquid Water Formation and Transport in a Transparent Single-Serpentine PEM Fuel Cell." *Journal of Power Sources* 170, no. 2 (2007): 334–44. https://doi.org/10.1016/j.jpowsour.2007.04.020.

[32] Spernjak, Dusan, Ajay K. Prasad, and Suresh G. Advani. “In Situ Comparison of Water Content and Dynamics in Parallel, Single-Serpentine, and Interdigitated Flow Fields of Polymer Electrolyte Membrane Fuel Cells.” *Journal of Power Sources* 195, no. 11 (2010): 3553–68. https://doi.org/10.1016/j.jpowsour.2009.12.031.

[33] Ding, Quan, Hong-Liang Zhao, Zhong-Min Wan, Yan-Ru Yang, Chen Yang, and Xiao-Dong Wang. “Performance of Parallel, Interdigitated, and Serpentine Flow Field PEM Fuel Cells with Straight or Wavelike Channels.” *Journal of Energy Engineering* 146, no. 5 (2020): 04020054. https://doi.org/10.1061/(asce)ey.1943-7897.0000701.

[34] Yin, Yan, Xiang Shangguan, Xiaoqiang Ma, Junfeng Zhang, and Yanzhou Qin. “Influence of Corner Structure of Fuel Cell Serpentine Channel on Water Removal.” *International Journal of Hydrogen Energy* 45, no. 54 (2020): 29812–23. https://doi.org/10.1016/j.ijhydene.2019.08.200.

[35] Kerkoub, Youcef, Ahmed Benzaoui, Fadila Haddad, and Yasmina K. Ziari. “Channel to Rib Width Ratio Influence with Various Flow Field Designs on Performance of PEM Fuel Cell.” *Energy Conversion and Management* 174 (2018): 260–75. https://doi.org/10.1016/j.enconman.2018.08.041.

[36] Zhang, Yuzhou, Viral Hirpara, Virat Patel, Chen Li, Ryan Anderson, Ning Zhu, and Lifeng Zhang. “Imaging of Desaturation of the Frozen Gas Diffusion Layers by Synchrotron X-Ray Radiography.” *International Journal of Hydrogen Energy*, 2021. https://doi.org/10.1016/j.ijhydene.2021.02.197.

[37] Rashapov, Rinat R., Jonathan Unno, and Jeff T. Gostick. “Characterization of PEMFC Gas Diffusion Layer Porosity.” *Journal of The Electrochemical Society* 162, no. 6 (2015). https://doi.org/10.1149/2.0921506jes.

[38] Vogelgesang, Matthias, Suren Chilingaryan, Tomy dos_Santos Rolo, and Andreas Kopmann. “UFO: A Scalable GPU-Based Image Processing Framework for On-Line Monitoring.” *2012 IEEE 14th International Conference on High Performance Computing*

and Communication & 2012 IEEE 9th International Conference on Embedded Software and Systems, 2012. https://doi.org/10.1109/hpcc.2012.116.

[39] Vogelgesang, Matthias, Tomas Farago, Thilo F. Morgeneyer, Lukas Helfen, Tomy dos Santos Rolo, Anton Myagotin, and Tilo Baumbach. "Real-Time Image-Content-Based Beamline Control for Smart 4D X-Ray Imaging." *Journal of Synchrotron Radiation* 23, no. 5 (2016): 1254–63. https://doi.org/10.1107/s1600577516010195.

[40] Wysokinski, Tomasz W., Dean Chapman, Gregg Adams, Michel Renier, Pekka Suortti, and William Thomlinson. "Beamlines of the Biomedical Imaging and Therapy Facility at the Canadian Light Source—Part 1." *Nuclear Instruments and Methods in Physics Research Section A: Accelerators, Spectrometers, Detectors and Associated Equipment* 582, no. 1 (2007): 73–76. https://doi.org/10.1016/j.nima.2007.08.087.

Chapter 5. Conclusions and Recommendations

5.1 Conclusions

The thawing and desaturation processes of the air purging cold-start GDLs were visualized via high speed, high resolution synchrotron X-ray CT. Based on the captured images, the dynamic saturation profiles and desaturation rates were analyzed qualitatively and quantitatively at both global and local scales of the GDL samples investigated in this project.

At the global scale, three thawing/desaturation phases were observed from the desaturation profile: GDL warm-up, partial thawing with water removal, and desaturation after complete thawing. The trends were similar in all the experimental cases. The air purging rate had a major effect on the thawing and desaturation process. At a higher purge rate, the desaturation rate of the GDLs is faster. GDL hydrophobicity did not show a significant effect on the desaturation process, but was found to affect the initial saturation level of the GDL samples. Also, heterogeneity was observed through the entire GDL domain both in-plane and through-plane, where water accumulation spots, slow desaturation regions, and uneven desaturated GDL layers were found in various GDL locations. Saturation contours, histograms, and 3D geometry models show that the level of local water blockage in a GDL can vary substantially, indicating that the GDL water management cannot be precisely characterized by the overall saturation value alone.

At the local scale, multiple segmentation levels were applied on the GDL in-plane to analyze the localized GDL thawing and desaturation processes. Like what has been found at the global scale, the similar trends were found in all the areas for each segmentation level. By selecting the whole channel region and the rib region as the area of interest, no significant difference was observed between the two geometries. Zooming into smaller segments, both the temporal desaturation profiles and the spatial saturation colormaps show that the purging distance, flow field geometry, and the initial saturation level all play important roles in the GDL thawing and desaturation process, with a longer purging distance and bend channel structures decreasing the thawing speed. Heterogeneity in water transfer becomes more evident at the local scale, which could even be found in the neighboring regions.

Both analyses in the global and local scales show the significant heterogenous behavior in the GDL thawing and desaturation process. It is necessary to focus on the water transfer behavior in the localized GDL regions in order to understand the behavior over the entire GDL domain. The results from this project provide valuable information for understanding the GDL water management during the cold-start process and could be used in optimizing the future experiments, modeling, and commercialized PEM fuel cell design.

5.2 Recommendations

A few challenges in the experimental sections of this research had not been addressed due to the limitation of resources and apparatus, which could possibly be solved in the future studies.

First, the cell temperature during the experiments was not controlled. The test cell was exposed to room temperature as soon as leaving the freezer. If the cell temperature is maintained at low temperature via external cooling such as cold coolant circulation, the thawing and desaturation process could be slowed down for better temporal resolution. Furthermore, if the cell temperature could be adjusted during the CT scanning, a better freezing process could be applied to simulate the actual cold-start process, enabling the water behavior study during the freezing process.

Secondly, the liquid water and ice were not clearly distinguished from each other in the CT images due to a subtle contrast difference. This limits the quantitative analysis of the thawing process and it requires further study through improving the synchrotron setup.

Finally, the same GDL samples were repeatedly used during the experiments. It was observed that as the same GDL samples experienced more water injection and freezing/thawing cycles, the initial saturation of that GDL sample increased. In consequence, the initial saturation levels for the same type of the GDL were not identical in each experiment. It can be solved by changing a new sample after each experimental trial.

Appendix A. Sample codes for image processing and calculations

The following sample code is written in ImageJ macro language. A table containing the overall GDL porosity for each CT slice in an experimental trial will be generated in the form of CSV.

```
run("Clear Results");

folderFirst=1;
folderLast=18;
folderName="35AA-10";

folderDirection="D:/2020-02/Thawing_CT_GDL/" + folderName+"/";
imageFirst=0;
imageLast=29;
saveDirection="D:/2020-02/Thawing_CT_GDL/" + folderName+"/";
threshold=-7E-4;

for (a=folderFirst+1; a<=folderLast; a++) {
	if (a==folderFirst+1) {
		cond="-freeze/";
	} else if (a==folderLast) {
		cond="-dry/";
	} else {
		cond="-thaw/";
	}
	for (b=imageFirst; b<=imageLast; b++) {
		open(folderDirection+a+cond+b+".tif");
		makeOval(70,70,1800,1800);
		getMinAndMax(min, max);
		nBins=(max-min)/0.000001;
		thresholdBins=(threshold-min)/0.000001;
		nBins=round(nBins);
```

```
                thresholdBins=round(thresholdBins);
                voidPixel=0;
                totalPixel=0;
                getHistogram(values,counts,nBins,min,max);
                for (c=0; c<nBins; c++) {
                        if (c<=thresholdBins) {
                                voidPixel=voidPixel+counts[c];
                                totalPixel=totalPixel+counts[c];
                        } else {
                                totalPixel=totalPixel+counts[c];
                        }
                }
                porosity=voidPixel/totalPixel;
                row=a-folderFirst;
                setResult(b, row, porosity);
                close();
        }
}
updateResults();
saveAs("Results", saveDirection+folderName+".csv");
```

The following sample code is written in Typescript with Deno runtime system. Each CSV files containing the porosity values for all the segments in each CT slice will be computed into the averaged saturation and averaged water content observed in each CT scan.

```
export function readCSV(folderPath: string, fileName: string, fileCount: number){
   const rawCSV = Deno.readTextFileSync(folderPath + '/' + fileName + '-' + fileCount + '.csv');
   const rows = rawCSV.split('\n');
   const csv = rows
      .filter((row) => row)
      .map((row) => row.split(','));
   csv.shift();
```

```
    csv.forEach((row, rowIndex) => row.shift());

    return csv;
}

export function writeCSV(folderPath: string, fileName: string,  csvText:any) {
    Deno.writeTextFileSync(folderPath + '/' + fileName + '.csv',csvText);
}

import { readCSV } from "./read-csv.ts";
import { writeCSV } from "./write-csv.ts";

const folderPath = Deno.args[0];
const fileName = Deno.args[1];
const fileCount = +Deno.args[2];

const dryGDLGroup = readCSV(folderPath, fileName, fileCount);
let convertedSaturationCSV: string = "";
let convertedDesaturationCSV: string = "";

for (let i = 1; i < fileCount; i++) {
    const wetGDLGroup = readCSV(folderPath, fileName, i);
    const saturationDifference: number[][] = [];
    const desaturationDifference: number[][] = [];
    wetGDLGroup.forEach((row, rowIndex) => {
        saturationDifference[rowIndex] = [];
        desaturationDifference[rowIndex] = [];
        row.forEach((column, columnIndex) => {
            let waterDifference = +dryGDLGroup[rowIndex][columnIndex] - (+column);
            if (waterDifference < 0) {
                waterDifference = 0;
```

```
        };
        saturationDifference[rowIndex][columnIndex] = waterDifference / (+dryGDLGroup[rowIndex][c
olumnIndex]);
        desaturationDifference[rowIndex][columnIndex] = waterDifference;
      });
    });

    const saturationAverage: number[] = [];
    saturationDifference.forEach((row, rowIndex) => {
      saturationAverage[rowIndex] = +0;
      for (let j = 0; j < row.length; j++) {
        saturationAverage[rowIndex] += saturationDifference[rowIndex][j];
      };
      saturationAverage[rowIndex] /= row.length;
    });

    const desaturationAverage: number[] = [];
    desaturationDifference.forEach((row, rowIndex) => {
      desaturationAverage[rowIndex] = +0;
      for (let j = 0; j < row.length; j++) {
        desaturationAverage[rowIndex] += desaturationDifference[rowIndex][j];
      };
      desaturationAverage[rowIndex] /= row.length;
    });

    let convertingSaturationCsv: string = saturationAverage.toString();
    convertedSaturationCSV += convertingSaturationCsv + "\n";

    let convertingDesaturationCsv: string = desaturationAverage.toString();
    convertedDesaturationCSV += convertingDesaturationCsv + "\n";

};
```

```
writeCSV(folderPath, fileName + "-Saturation", convertedSaturationCSV);
writeCSV(folderPath, fileName + "-Desaturation", convertedDesaturationCSV);
```

Appendix B. Construction of the 3-D geometry models

The 3-D geometry models shown in this work were constructed using Avizo 9.3, based on the reconstructed CT images. As shown in Figure B.1, these slices of images were cropped into a smaller size (3.18 mm x 3.18 mm) containing the area of interest, and were converted into 8-bit images, due to the limitation in the computing power. For the images taken in a single scan, all the image slices were inputted into Avizo as a stack to generate a basic 3-D model. Then, the non-vacant volume (mixture of GDL structure and water content) was segmented by tuning the threshold. The same process was also performed on images of the dry state GDL, where the non-vacant volume is equal to the GDL structure, colored in grey. By subtracting this volume from the mixture, the total volume of the water content would be obtained, colored in light blue. The combination of these two segments in a 3-D model is shown in Figure B.2. For better demonstration on the water distribution, the top half of the GDL structure was hidden.

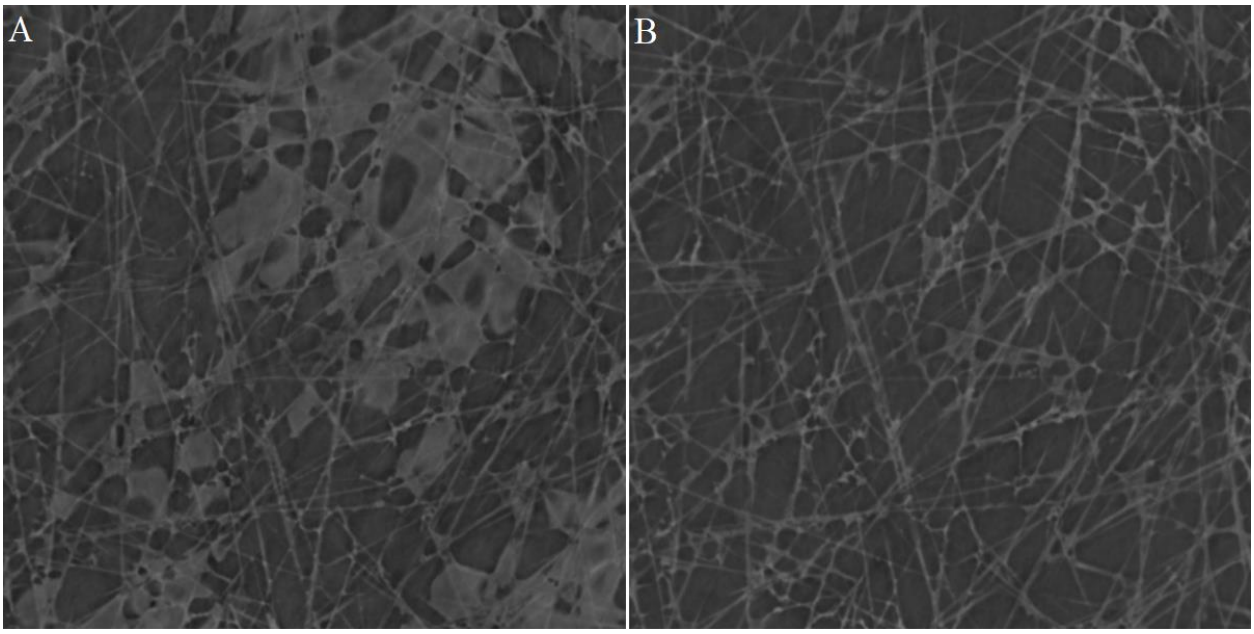

Figure B.1. A sample slice of image in the area of interest at the same geometry location for A) 0 minute thawing and B) dry state.

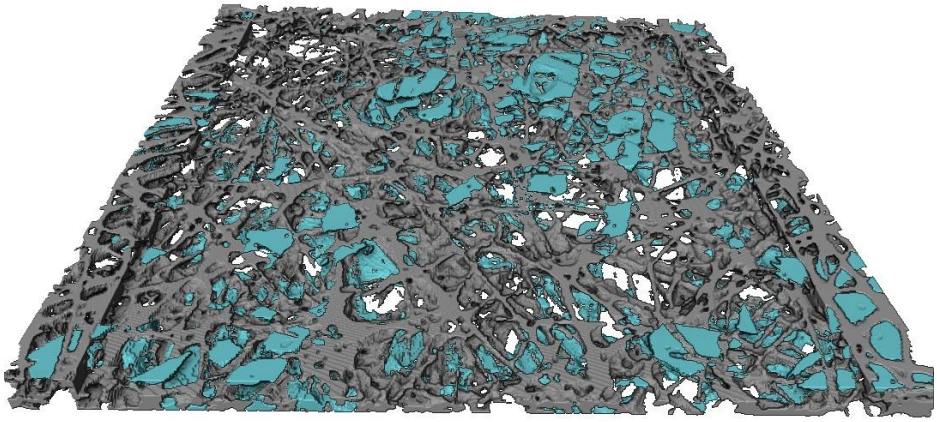

Figure B.2. The 3-D geometry model based on the slices shown in Figure B.1 for 0 minute thawing.

Appendix C. Copyright forms

ELSEVIER LICENSE TERMS AND CONDITIONS

May 04, 2021

This Agreement between University of Saskatchewan -- Yuzhou Zhang ("You") and Elsevier ("Elsevier") consists of your license details and the terms and conditions provided by Elsevier and Copyright Clearance Center.

License Number	5062151245664
License date	May 04, 2021
Licensed Content Publisher	Elsevier
Licensed Content Publication	Journal of Power Sources
Licensed Content Title	Passive control of liquid water storage and distribution in a PEFC through flow-field design
Licensed Content Author	A. Turhan,K. Heller,J.S. Brenizer,M.M. Mench
Licensed Content Date	Jun 1, 2008
Licensed Content Volume	180
Licensed Content Issue	2
Licensed Content Pages	11
Start Page	773
End Page	783
Type of Use	reuse in a thesis/dissertation
Portion	figures/tables/illustrations
Number of figures/tables/illustrations	1
Format	electronic
Are you the author of this Elsevier article?	No
Will you be translating?	No
Title	Visualization of Thawing and Desaturation in Frozen Gas Diffusion Layers of Proton Exchange Membrane Fuel Cells via Synchrotron X-ray Radiography
Institution name	University of Saskatchewan
Expected presentation date	May 2021
Portions	Fig 3
Requestor Location	University of Saskatchewan 105 Administration Place Saskatoon, SK S7N 5A2 Canada Attn: University of Saskatchewan
Publisher Tax ID	GB 494 6272 12
Total	**0.00 USD**

ELSEVIER LICENSE
TERMS AND CONDITIONS

May 04, 2021

This Agreement between University of Saskatchewan -- Yuzhou Zhang ("You") and Elsevier ("Elsevier") consists of your license details and the terms and conditions provided by Elsevier and Copyright Clearance Center.

License Number	5062151082025
License date	May 04, 2021
Licensed Content Publisher	Elsevier
Licensed Content Publication	International Journal of Hydrogen Energy
Licensed Content Title	3D classification of polymer electrolyte membrane fuel cell materials from in-situ X-ray tomographic datasets
Licensed Content Author	Utku U. Ince,Henning Markötter,Nan Ge,Merle Klages,Jan Haußmann,Martin Göbel,Joachim Scholta,Aimy Bazylak,Ingo Manke
Licensed Content Date	Apr 17, 2020
Licensed Content Volume	45
Licensed Content Issue	21
Licensed Content Pages	9
Start Page	12161
End Page	12169
Type of Use	reuse in a thesis/dissertation
Portion	figures/tables/illustrations
Number of figures/tables/illustrations	1
Format	electronic
Are you the author of this Elsevier article?	No
Will you be translating?	No
Title	Visualization of Thawing and Desaturation in Frozen Gas Diffusion Layers of Proton Exchange Membrane Fuel Cells via Synchrotron X-ray Radiography
Institution name	University of Saskatchewan
Expected presentation date	May 2021
Portions	Fig 6
Requestor Location	University of Saskatchewan 105 Administration Place Saskatoon, SK S7N 5A2 Canada Attn: University of Saskatchewan
Publisher Tax ID	GB 494 6272 12
Total	**0.00 USD**

Copyright Clearance Center Marketplace™

IOP Publishing, Ltd - License Terms and Conditions

This is a License Agreement between Yuzhou Zhang ("You") and IOP Publishing, Ltd ("Publisher") provided by Copyright Clearance Center ("CCC"). The license consists of your order details, the terms and conditions provided by IOP Publishing, Ltd, and the CCC terms and conditions.

All payments must be made in full to CCC.

Order Date	04-May-2021	Type of Use	Republish in a thesis/dissertation
Order license ID	1116521-1	Publisher	IOP Publishing
ISSN	0013-4651	Portion	Image/photo/illustration

LICENSED CONTENT

Publication Title	Journal of the Electrochemical Society	Rightsholder	IOP Publishing, Ltd
Article Title	Liquid-Water Interactions with Gas-Diffusion-Layer Surfaces	Publication Type	Journal
Author/Editor	ELECTROCHEMICAL SOCIETY.	Start Page	F1184
Date	12/31/1947	End Page	F1193
Language	English	Issue	12
Country	United States of America	Volume	161

REQUEST DETAILS

Portion Type	Image/photo/illustration	Distribution	Canada
Number of images / photos / illustrations	1	Translation	Original language of publication
Format (select all that apply)	Electronic	Copies for the disabled?	No
Who will republish the content?	Academic institution	Minor editing privileges?	No
Duration of Use	Current edition and up to 5 years	Incidental promotional use?	No
Lifetime Unit Quantity	Up to 499	Currency	CAD
Rights Requested	Main product		

NEW WORK DETAILS

Title	Visualization of Thawing and Desaturation in Frozen Gas Diffusion Layers of Proton Exchange Membrane Fuel Cells via Synchrotron X-ray Radiography	Institution name	University of Saskatchewan
		Expected presentation date	2021-05-07
Instructor name	Yuzhou Zhang		

ADDITIONAL DETAILS

Order reference number	N/A	The requesting person / organization to appear on the license	Yuzhou Zhang

REUSE CONTENT DETAILS

Title, description or numeric reference of the portion(s)	Fig 2	Title of the article/chapter the portion is from	Liquid-Water Interactions with Gas-Diffusion-Layer Surfaces
Editor of portion(s)	Santamaria, A. D.; Das, P. K.; MacDonald, J. C.; Weber, A. Z.	Author of portion(s)	Santamaria, A. D.; Das, P. K.; MacDonald, J. C.; Weber, A. Z.
Volume of serial or monograph	161	Issue, if republishing an article from a serial	12
Page or page range of portion	F1184-F1193	Publication date of portion	2014-08-20

Copyright Clearance Center Marketplace™

Royal Society of Chemistry - License Terms and Conditions

This is a License Agreement between Yuzhou Zhang ("You") and Royal Society of Chemistry ("Publisher") provided by Copyright Clearance Center ("CCC"). The license consists of your order details, the terms and conditions provided by Royal Society of Chemistry, and the CCC terms and conditions.

All payments must be made in full to CCC.

Order Date	04-May-2021	Type of Use	Republish in a thesis/dissertation
Order license ID	1116505-1	Publisher	ROYAL SOCIETY OF CHEMISTRY
ISSN	1463-9084	Portion	Image/photo/illustration

LICENSED CONTENT

Publication Title	Physical chemistry chemical physics	Country	United Kingdom of Great Britain and Northern Ireland
Author/Editor	Royal Society of Chemistry (Great Britain)	Rightsholder	Royal Society of Chemistry
Date	12/31/1998	Publication Type	e-Journal
Language	English	URL	http://firstsearch.oclc.org/journal=1463-9076;screen=info;ECOIP

REQUEST DETAILS

Portion Type	Image/photo/illustration	Distribution	Canada
Number of images / photos / illustrations	1	Translation	Original language of publication
		Copies for the disabled?	No
Format (select all that apply)	Electronic	Minor editing privileges?	No
Who will republish the content?	Academic institution	Incidental promotional use?	No
Duration of Use	Current edition and up to 5 years	Currency	CAD
Lifetime Unit Quantity	Up to 499		
Rights Requested	Main product		

NEW WORK DETAILS

Title	Visualization of Thawing and Desaturation in Frozen Gas Diffusion Layers of Proton Exchange Membrane Fuel Cells via Synchrotron X-ray Radiography	Institution name	University of Saskatchewan
		Expected presentation date	2021-05-07
Instructor name	Yuzhou Zhang		

ADDITIONAL DETAILS

Order reference number	N/A	The requesting person / organization to appear on the license	Yuzhou Zhang

REUSE CONTENT DETAILS

Title, description or numeric reference of the portion(s)	Fig 3	Title of the article/chapter the portion is from	The influence of membrane electrode assembly water content on the performance of a polymer electrolyte membrane fuel cell as investigated by 1H NMR microscopy
Editor of portion(s)	N/A		
Volume of serial or monograph	N/A		
Page or page range of portion	1852	Author of portion(s)	Royal Society of Chemistry (Great Britain)
		Issue, if republishing an article from a serial	N/A
		Publication date of portion	2007-02-07